

AD-A128 766

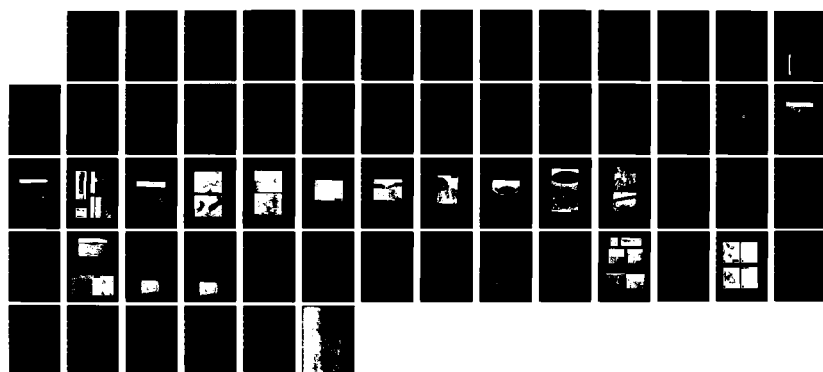
SURFACE MELTING AND ALLOYING OF METALS BY THE CO₂ LASER 1/1
(U) BATTELLE COLUMBUS LABS OH A H CLAUER ET AL.

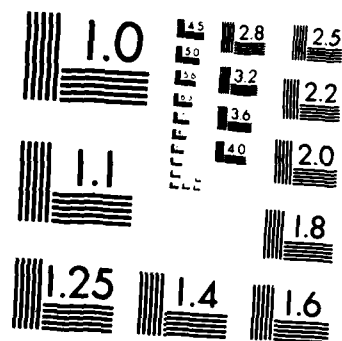
29 APR 83 DAAG29-79-C-0065

UNCLASSIFIED

F/G 11/6

NL





MICROCOPY RESOLUTION TEST CHART
NATIONAL BUREAU OF STANDARDS 1963 A

ARO 16296.5-MS
(12)

AD A 128 766

SURFACE MELTING AND ALLOYING OF
METALS BY THE CO₂ LASER

FINAL REPORT

A. H. Clauer, C. T. Walters, and T. R. Tucker

April 29, 1983

U. S. ARMY RESEARCH OFFICE

DAAG29-79-C-0065

BATTELLE
Columbus Laboratories
505 King Avenue
Columbus, Ohio 43201

APPROVED FOR PUBLIC RELEASE
DISTRIBUTION UNLIMITED
J

DMC FILE COPY

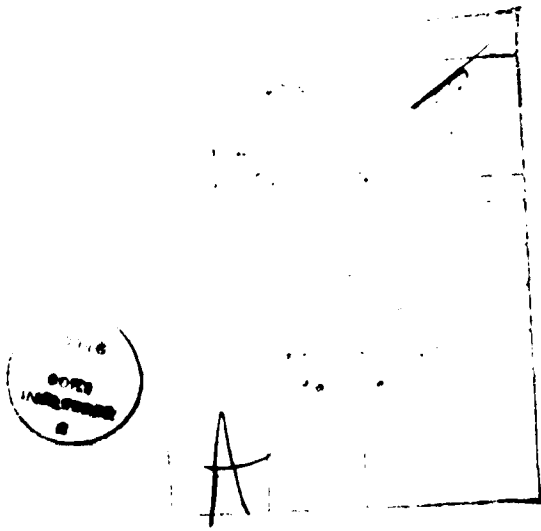
~~Unclassified~~

SECURITY CLASSIFICATION OF THIS PAGE (When Data Entered)

REPORT DOCUMENTATION PAGE		READ INSTRUCTIONS BEFORE COMPLETING FORM
1. REPORT NUMBER	2. GOVT ACCESSION NO.	3. RECIPIENT'S CATALOG NUMBER
4. TITLE (and Subtitle) Surface Melting and Alloying of Metals by the CO ₂ Laser		5. TYPE OF REPORT & PERIOD COVERED Final Report, 6/15/79-10/31/82
		6. PERFORMING ORG. REPORT NUMBER
7. AUTHOR(s) A. H. Clauer		8. CONTRACT OR GRANT NUMBER(s) DAAG29-79-C-0065
9. PERFORMING ORGANIZATION NAME AND ADDRESS Battelle Columbus Laboratories 505 King Avenue Columbus, Ohio 43201		10. PROGRAM ELEMENT, PROJECT, TASK AREA & WORK UNIT NUMBERS
11. CONTROLLING OFFICE NAME AND ADDRESS U. S. Army Research Office Ft. Monmouth, Box 12001 Research Triangle Park, NC 27709		12. REPORT DATE 29 April 1983
		13. NUMBER OF PAGES
14. MONITORING AGENCY NAME & ADDRESS (if different from Controlling Office)		15. SECURITY CLASS. (of this report) Unclassified
		15a. DECLASSIFICATION/DOWNGRADING SCHEDULE
16. DISTRIBUTION STATEMENT (of this Report) Approved for public release; distribution unlimited.		
17. DISTRIBUTION STATEMENT (of the abstract entered in Block 20, if different from Report)		
18. SUPPLEMENTARY NOTES THE VIEW, OPINIONS, AND/OR FINDINGS CONTAINED IN THIS REPORT ARE THOSE OF THE AUTHOR(S) AND SHOULD NOT BE CONSTRUED AS AN OFFICIAL DEPARTMENT OF THE ARMY POSITION, POLICY, OR DECISION, UNLESS SO DESIGNATED BY OTHER DOCUMENTATION.		
19. KEY WORDS (Continue on reverse side if necessary and identify by block number) Laser Melting, Laser Alloying, Laser-Material Interaction, Laser Energy Absorption, Cast Iron, Iron-Molybdenum-Carbon		
20. ABSTRACT (Continue on reverse side if necessary and identify by block number) This report describes a program which investigateded the laser-material interactions for pulsed and continuous wave CO ₂ lasers with iron and iron-4 wt.% carbon surfaces. The thermal coupling coefficient of pure iron increased with increasing laser fluence, with the most significant increase occurring just before the damage threshold. The iron-carbon alloy had a higher coupling coefficient which was relatively		
(continued on reverse)		

20. Abstract (Continued)

independent of fluence. The pulsed and CW CO₂ lasers were also used to surface melt cast irons. Very short interaction times developed thin, rapidly solidified featureless melts on the cast iron surfaces. These layers were identified as a carbon saturated epsilon phase. In addition, laser surface alloying of Fe-0.8C, Fe-1.4C and Fe-2.8C alloys with Mo was studied. The resulting melt layers were generally chemically uniform and showed the presence of ferrite, martensite, and Mo₂C and an M₆C carbide.



STATEMENT OF THE PROBLEM

This study addressed two areas of laser surface melting and alloying: the mechanism of the interaction of the laser beam with a metal surface as it effects the energy transfer to the work surface; and the physical metallurgy of the laser melted surfaces of iron-carbon and laser alloyed surfaces of molybdenum on iron-carbon.

SUMMARY OF IMPORTANT RESULTS

This program studied the effects of both pulsed and continuous wave CO₂ lasers on the mechanisms of the laser material interaction and on the physical metallurgy of the melt layers. For thin, rapidly solidified melt layers, the short interaction times associated with a pulsed laser beam onto a surface may provide some advantages in microstructure and properties. In addition, because the workpiece can be stationary during the beam interaction time, the set-up and sample geometry are conducive to diagnostics of the energy balance around the coupling of the laser energy into the workpiece. This enabled the thermal coupling coefficient for the laser material interaction to be determined. The thermal coupling coefficient is simply the total energy retained in the target sample through absorption divided by the incident energy.

The thermal coupling coefficients for TEA CO₂ laser pulses were reported for the first time for pure iron and iron-4 weight percent carbon alloy surfaces⁽¹⁾. The variation of the thermal coupling coefficient for both the iron and iron-4 carbon alloys is shown in Ref. 1, App. A. For the pure iron, the coupling coefficient initially increases slightly as expected from thermal affects manifested in increased electron coupling. Near 19 joules/cm², however, a dramatic rise in thermal coupling with increasing fluence was first observed. The D on the curve indicates that damage, as a very sudden change in the surface, was first observed at this point. As the fluence increased above the damage threshold, thermal

coupling increased but at a reduced slope. At the point marked P on the curve, at 45 joules/cm, plasma luminosity was first observed. This apparently enhanced the thermal coupling as noted in the figure. At a fluence of 80 joules/cm², the coupling reached 14 percent, which is a factor of six greater than the room temperature value. Material removal was detected by a vapor deposition gauge at 60 joules/cm².

The data for the iron-carbon alloy shows higher thermal coupling coefficients over the entire range of fluences investigated. The polished iron-carbon surface indicates an as-cast surface which contains a relatively heterogeneous dendritic structure consisting of iron-carbide and ferrite intersecting the specimen surface. This surface has a thermal coupling coefficient of about 9 percent, which compared to the pure iron indicates a strong affect of the presence of carbon on absorptivity. For a similar sample that had been laser surface melted to refine and homogenize the surface, the thermal coupling is twice as high at low fluence levels as that of the non-homogenized surface. The surface of the laser treated sample was oxidized and therefore not free of defects as was the polished surface. In this case, above the damage threshold, the thermal coupling decreased with increasing fluence. This suggests that clean-up of the surface probably dominated any thermal effects. In addition, the plasma initiated below the damaged threshold, which is typical of defect initiated plasmas.

It was concluded through an analysis that the dramatic rise of the thermal coupling coefficient to a factor of three greater than the low fluence value for fluences less than the plasma threshold, could not be attributed to plasma enhancement. Neither do the details of the variation of coupling with fluence correlate well with a thermal model based on a simple (free electron) Drude theory, but instead seem to require a non-linear effect to be evoked. When alloying constituents are added to iron, this effect proves to be masked by the impurity constituents associated with the alloy additions. In the case of alloys, coupling is higher and much less fluence dependent.

Laser Surface Melting of Cast Irons

The program also investigated the microstructures developed in laser surface melted white and gray cast irons⁽²⁾ and the microstructure in the surface layers of laser alloyed iron-carbon-molybdenum surfaces⁽³⁾. The gray and white irons investigated contained 4.2 weight percent carbon with either 1 weight percent silicon (gray cast) or no silicon (white cast). Both continuous and pulsed CO₂ laser interactions were studied. For these studies, the microstructures and phases in the heat affected zones and fusion zones were analyzed and compared to the as-cast starting material. The continuous wave CO₂ homogenizing passes ranged from 50 to 500 μm deep and the pulsed CO₂ radiation resulted in melt layers 5 to 7 μm thick. As expected, the homogenizing treatment on the gray cast iron produced refined white cast surface layers. There was some tendency to crack, but it is much lower than that observed in white cast iron.

If on top of the homogenizing deeper passes that were made on the white cast iron, a pulsed CO₂ laser interaction is applied, a very thin 3 to 7 μm deep rapidly solidified layer is produced. This 5 μm thick layer appears featureless even at 10,000 magnification. Transmission electron microscopy and x-ray study of this rapidly solidified layer revealed it to have a cellular structure consisting primarily of a carbon saturated epsilon phase, containing about 4.2 weight percent carbon, about the same carbon level as the original casting. The hardness level was intermediate between the underlying heat affected zone and the original hardness, indicating that it was not a super hard phase such as high carbon martensite.

In the surface melting of the gray cast iron, the cast layer, by the nature of being more rapidly solidified, is a white cast iron. Deeper homogenizing passes are required in gray cast iron to ensure that the graphite flakes have been dissolved and homogenization is actually achieved. In the gray cast iron as in the white cast iron, a thin rapidly solidified layer, in this case produced by a rapidly scanned CW CO₂ laser beam, again developed a featureless melt.

This work in the cast irons was among the first to indicate the white cast layer formed on gray cast irons, but more importantly, to show the presence of the featureless layer of epsilon phase represented by the rapidly solidified thin melt region. The supersaturated epsilon phase is a microstructure similar to that reported in splat-quenched iron-carbon alloys having similar carbon content.

Laser Surface Alloying of Molybdenum on Iron-Carbon Substrates

Surface alloying with molybdenum of iron-carbon substrates containing three levels of carbon, 0.8, 1.4, and 2.8 weight percent carbon was investigated⁽³⁾. The objective of this part of the study was to utilize the hard carbide hardening properties of the molybdenum in the same way it is employed in conventional tool steels. The different carbon contents of the iron substrates enabled this effect on the solidification structures to also be investigated to some extent. The molybdenum was applied by plasma spraying before laser alloying. The laser beam was then used to melt the molybdenum layer into the iron-carbon substrate to form an iron-carbon-molybdenum alloy surface. A rectangular beam shape with a shaped beam intensity profile was used to minimize overlap affects between neighboring laser passes when performing area coverage.

Examination and analysis of the laser surface melt layers revealed several points. One of these is that in a shallow melt pass, it was revealed that the melting in this case proceeded from the interface between the molybdenum and iron and proceeded outward towards the surface. The sequence of melting appeared to develop more homogeneous melt layer compositions than did higher intensity passes which melted from the surface inward.

The microstructures of the melt layers showed at least three phases. The solidification in the alloy layer formed on the 0.8 carbon substrate showed cellular solidification. The distribution of molybdenum

was relatively uniform through the melt thickness ranging from 33 weight percent at the top to 29 weight percent at the bottom. This is of a melt layer approximately 1 mm thick. Of the two phases present, one of these contained nominally 34 weight percent molybdenum and the other about 15 weight percent molybdenum. It is expected that these microstructures would consist of δ -ferrite and austenite. Any carbides present were too small to be resolved.

The melt layers formed on the 1.4 and 2.8 carbon-containing substrates developed dendritic solidification patterns instead of the cellular pattern. X-ray diffraction study of the iron-2.8 carbon sample revealed three prominent phases -- alloyed ferrite, tetragonal martensite, and a hexagonal carbide similar to Mo_2C . A cubic M_6C was also detected. The martensite was present only in the heat affected overlap zones between neighboring passes. It is possible that this occurred by transformation of austenite that had precipitated out carbide while at higher temperatures in the heat affected zone.

Hardness measurements in the laser alloyed melt regions indicated that alloying with molybdenum did increase the hardness significantly for each of the three carbon-containing substrates. However, the hardness was not increased to the level often observed in fully heat treated tool steels. This might be possible if post-laser heat treatments had been used.

APPENDIX

PUBLICATIONS

APPENDIX

LIST OF PUBLICATIONS

- (1) Walters, C. T., Tucker, T. R., Ream, S. L., Clauer, A. H., and Gallant, D. J., "Thermal Coupling of CO₂ Laser Radiation to Metals". Published in Lasers in Metallurgy, ed. by H. Mukherjee and J. Mazumder, The Metallurgical Society of AIME, Warrendale, Pennsylvania (1981).
- (2) Tucker, T. R., Clauer, A. H., and McCall, J. L., "Microstructures of Laser Surface Melted White and Gray Cast Irons". Published in Microstructural Science, Vol. 10, ed. by W. E. White and J. H. Richardson, Elsevier Science Publ. Co., Inc., New York (1982), pp. 347-358.
- (3) Tucker, T. R., Clauer, A. H., Ream, S. L., and Walters, C. T., "Rapidly Solidified Microstructure in Surface Layers of Laser-Alloyed Mo on Fe-C Substrates". Published in Rapidly Solidified Amorphous and Crystalline Alloys, ed. by B. H. Kear, B. C. Giessen, and M. Cohen, Elsevier Science Publ. Co., Inc., New York (1982), pp. 541-545.
- (4) Tucker, T. R., Clauer, A. H., Walters, C. T., and Ream, S. L., "Laser Surface Melting of Iron - 4.2 Wt. Pct. Carbon Alloy". Published in Lasers in Metallurgy, ed. by H. Mukherjee and J. Mazumder, The Metallurgical Society of AIME, Warrendale, Pennsylvania (1981).
- (5) Tucker, T. R., and Clauer, A. H., "Directed Energy Surface Processing of Metals". Published in Rapid Solidification Processing, Principles and Technologies, III, ed. by R. Mehrabian, B. Kear, and M. Cohen, Gaithersburg, Maryland (December 1982).

THERMAL COUPLING OF CO₂ LASER RADIATION TO METALS

C. R. Walters, T. R. Tucker, S. L. Beam,
A. H. Clauer, and D. J. Gallant
 Battelle, Columbus Laboratories
 505 King Avenue
 Columbus, Ohio 43201

Thermal coupling coefficients are reported for the first time for TEA CO₂ laser pulses (10.6 μ m) on pure iron and iron -4% carbon alloy surfaces. Large increases in the pure iron thermal coupling were observed with increasing fluence that were not attributable to plasma enhancement. Thermal modeling results are also reported which indicate that the details of the increase with increasing fluence cannot be correlated with a simple free-electron model of optical absorption. Iron alloy thermal coupling results are also presented which indicate less dependence on fluence but significant surface preparation effects.

Published in Lasers in Metallurgy, ed. by
H. Mukherjee and J. Mazumder, the Met. Soc.
of AIME, Warrendale, Pennsylvania (1981).

Introduction

The pulsed CO₂ laser has great potential for application to surface modification of metals. While pulsed device development lags that of continuous CO₂ lasers, it has been demonstrated that rapidly solidified surface layers can be produced in the pulsed mode which have an appearance similar to those produced by 5000 W continuous scanned beams. An example is shown in Figure 1 which presents a micrograph of a section through a rapidly solidified surface layer (white region 6 μm thick) produced on a cast Fe-4 wt% C by single TEA-CO₂ laser pulses incident at 71 J/cm².



Fig. 1 - Cross section of Fe-4C sample which has been surface melted with TEA laser pulses.

An important key to development of pulsed CO₂ laser processing of metals is an understanding of thermal coupling mechanisms operative on the surface of metals under various fluence and power density conditions. Thermal coupling is characterized by the thermal coupling coefficient which is simply the total energy retained in a target sample during a laser pulse divided by the incident energy. Research has been undertaken at Battelle (1-4) and elsewhere (5-12) to elucidate the details of thermal coupling, plasma effects, reflectivity transients, and microstructure changes in several materials. This paper presents the first experimental data on thermal coupling of CO₂ laser pulses to pure iron and an iron-carbon alloy. In prior work (3) it was discovered that pure iron exhibited an anomalous specular reflectivity transient similar to that discovered for aluminum (1) when subjected to intense CO₂ laser pulses in vacuum. In this transient, the specular reflectivity dropped to 35% of the initial value during a 70 ns pulse and recovered to full reflectivity prior to the end of the pulse. Open shutter photography revealed no surface luminosity indicative of plasma. To assess the extent to which the anomaly can be related to increased target absorption, thermal coupling measurements were initiated under conditions similar to those reported earlier (3).

Experimental Approach

Laser irradiations were conducted with 1.4 cm x 1.4 cm x 2-3 mm thick target samples mounted in a vacuum chamber as illustrated schematically in Figure 2. The beam from a Lumonics Model 301 TEA CO₂ laser was focused

SPOT-LOADED IRRADIANCE GEOMETRY

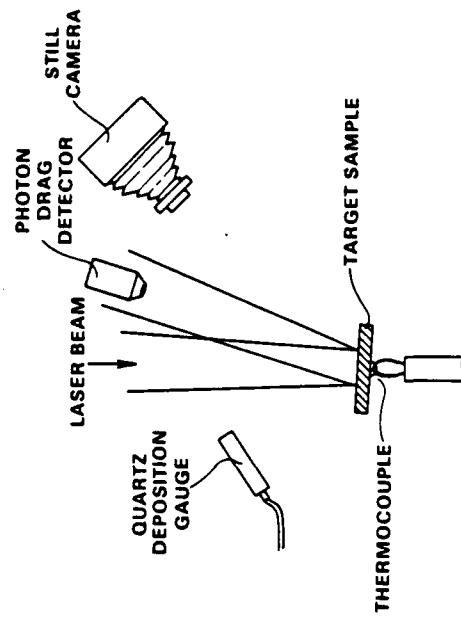


Fig. 2 - Experimental arrangement for thermal coupling measurements with spot-loaded irradiance geometry.

with a 1 m focal length germanium lens and was directed into the chamber through a sodium chloride optical flat which provided reflections for beam calorimetry external to the chamber. The target samples were instrumented with rear surface 30 gauge copper/constantan thermocouples which also served to support the sample with a minimum of thermal conduction loss.

The target samples were located slightly behind the focal plane where the beam spot was completely on the target (spot-loading conditions). The effective 1/e diameter of the spot was 0.7 cm (0.35 cm² effective area). The beam energy density profile was not uniform but could be characterized as a distorted Gaussian profile. The principal advantages of this arrangement were that the measurement of thermal coupling could be performed without sensitivity to beam alignment errors and without instrumentation difficulties associated with a small target which would be required for flood-loading geometry. Additionally, all luminosity in this arrangement could unambiguously be attributed to target effects. The disadvantage of this arrangement was the spatial integration of the measured effects as a result of the nonuniform energy density profile.

Sequences of CO₂ laser irradiations were conducted in vacuum for several iron and iron alloy samples with two different temporal pulse shapes as illustrated in Figure 3. The long pulse is the normal TEA laser pulse consisting of a gain-switched spike (70-100 ns FWHM) followed by a long low intensity tail lasting about 2 μs . The short pulse was obtained

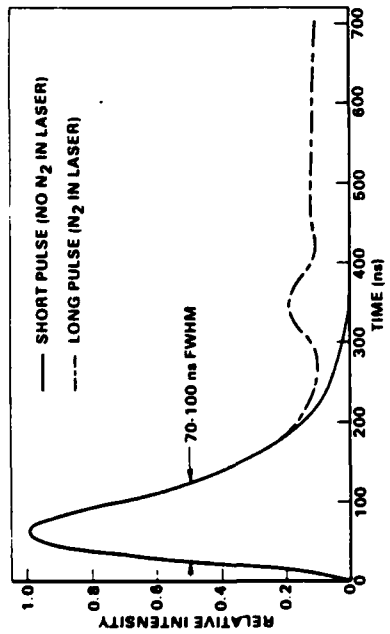


Fig. 3 - TEA laser pulse shapes.

by running the laser without nitrogen in the gas mix. Generally, samples were irradiated with a single pulse shape in a sequence of pulses of increasing fluence without sample movement or replacement. Thermocouple output was amplified and recorded with a strip chart recorder. The data were analyzed to obtain the equilibrium temperature rise in the sample from which the energy absorbed by the target in the interaction was computed. This value divided by the incident energy yielded the spatially and temporally averaged thermal coupling coefficient.

In addition to thermocouple data, simultaneous observations of plasma luminosity, reflectivity transients, and mass removal were recorded. Plasma luminosity was recorded with an open shutter camera ($f/4.7$) and ASA 400 speed Polaroid film. A photomultiplier detector was aligned in the specularly reflected beam to view the interaction area but definitive results were not anticipated because of spatial averaging of the reflected beam. An oscillating-quartz-disc thin-film deposition gauge was employed to detect vaporization of target material.

Experimental Results

Thermal coupling coefficients measured for mechanically polished pure iron samples are presented in Figures 4 and 5 for the long and short TEA CO₂ laser pulses, respectively. It is important to note that these coefficients are spatial averages for the irradiance pattern, but are plotted as a function of the spatial peak fluence. In Figure 4, all data were taken at the same surface location of the same sample with the long pulse. The open circles indicate the coefficient measured for the first pulse at a given fluence level in the sequence of increasing fluence levels while the solid circles indicate repeat pulses after the sample had been exposed to fluences higher than that indicated. Good agreement is noted between initial and repeat data at a given fluence, indicating a minimal effect of damage accumulation on thermal coupling. The dashed line is included to guide the eye along what is believed to be the trend in the data. Random scatter in the data is fairly small, but systematic error bounds due to calorimetry and profiling inaccuracy are estimated at $\pm 30\%$ for fluence and $\pm 20\%$ for coupling coefficient. The low fluence limit for thermal coupling appears to be near 2.2 J/cm^2 which is somewhat lower than that indicated by the limited room temperature $10.6 \mu\text{m}$ iron absorptance data available from the literature

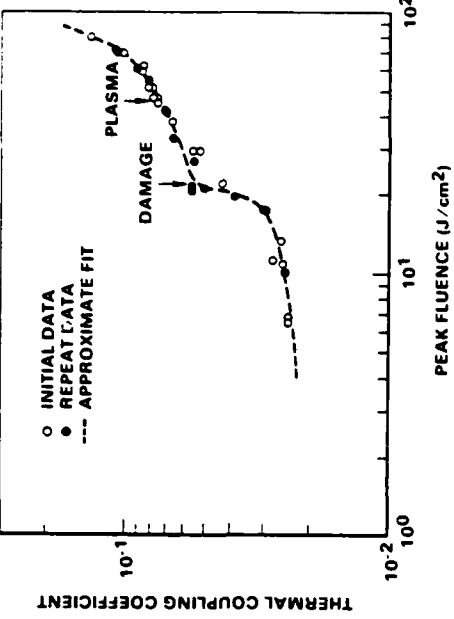


Fig. 4 - Thermal coupling coefficient for polished pure iron exposed to long TEA CO₂ laser pulse ($10.6 \mu\text{m}$) in vacuum.

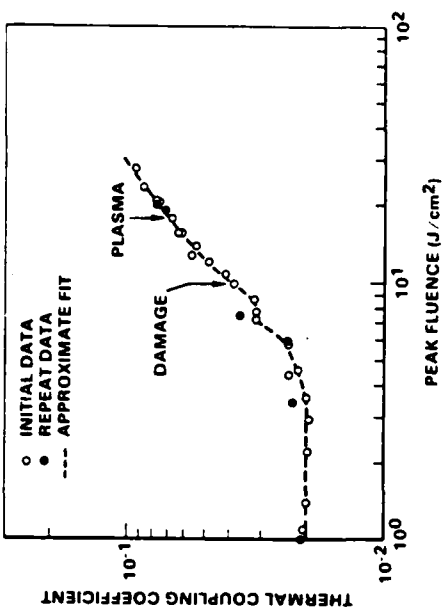


Fig. 5 - Thermal coupling coefficient for polished pure iron exposed to short TEA CO₂ laser pulse ($10.6 \mu\text{m}$) in vacuum.

($3.0\text{-}4.5\text{ J/cm}^2$) (13). The high degree of polish, sample cleaning, and vacuum environment may account for some of the difference. As peak fluence was increased the thermal coupling coefficient increased monotonically as might be expected simply from thermal effects as manifested in increased electron scattering. Near 19 J/cm^2 , however, a dramatic rise in thermal coupling with increasing fluence was observed. An arrow in the figure indicates where damage was first observed (21 J/cm^2). Damage in this case was a very subtle change in the surface as indicated by visual observation of the specularity

of the surface after each pulse as compared to that of unirradiated portions of the sample. It is important to note that no luminosity was observed to be associated with the large increase in coupling. As fluence was increased above the damage threshold, thermal coupling increased at a reduced slope. At 45 J/cm², plasma luminosity was first observed. The plasma apparently enhanced thermal coupling as noted in the figure at high fluences where the coefficient rises sharply again. At 80 J/cm² the coupling reached 14% which is a factor of 6 greater than the room temperature value. No definitive indication of the anomalous reflectivity effect was observed in the spatially integrated specular reflectivity signal at fluences below plasma threshold. Material removal was detected by the vapor deposition gauge at 60 J/cm².

Thermal coupling data for the short pulse are presented in Figure 5. Again the low fluence coefficient was found to be near 2% and a monotonic increase in coefficient with increasing fluence was observed. A small deviation from a smooth increase in coefficient was observed below damage threshold (9.8 J/cm²) but this may have been scatter in the data. The magnitude of increase of coupling was, however, still very significant below the plasma threshold (18 J/cm²). The effect of the shorter pulse appears to be reduction of the damage and plasma fluence thresholds by about a factor of two. This was expected because of the higher peak power density (at constant fluence) and associated more rapid heating and shallower melt depth.

Discussion of Results

It is of interest to see to what extent available theory can be used to explain the observed increases in thermal coupling of pure iron with increasing fluence. To this end, one-dimensional heat-conduction calculations were performed which characterized the pulsed laser/surface interaction. An explicit finite difference numerical model was assembled which employed:

- prescribed optical absorptance as a function of temperature,
- constant thermal conductivity,
- temperature-dependent heat capacity,
- heat of fusion,
- one-dimensional transient thermal conduction, and
- linearized laser pulse shape.

The critical input model, of course, was the function describing the optical absorptance variation with temperature. At low beam intensities it is reasonable to assume that the simple Drude (free-electron) theory of optical absorption in metals may be used as a starting point to describe the interaction. As pointed out by Wieting and Schriempf (14), however, even this assumption may be subject to question for metals such as nickel and iron where bound electrons may play a role. Lacking any better theory, free electrons were assumed for the calculation and the optical absorptivity, α , was computed as (14)

$$\alpha = \frac{4n}{(n+1)^2 + k^2}$$

where n is the index of refraction and k is the extinction index for the metal. These parameters are in turn related to the real and imaginary parts of the electrical conductivity, σ_1 and σ_2 , by

$$2n^2 = \left(1 - \frac{\sigma_2}{\omega\epsilon_0}\right) + \left[\left(1 - \frac{\sigma_2}{\omega\epsilon_0}\right)^2 + \left(\frac{\sigma_1}{\omega\epsilon_0}\right)^2\right]^{1/2} \quad (2)$$

$$2k^2 = -\left(1 - \frac{\sigma_2}{\omega\epsilon_0}\right) + \left[\left(1 - \frac{\sigma_2}{\omega\epsilon_0}\right)^2 + \left(\frac{\sigma_1}{\omega\epsilon_0}\right)^2\right]^{1/2} \quad (3)$$

where

$$\sigma_1 = \frac{\sigma_0}{(1+\omega^2\tau^2)} \quad (4)$$

$$\sigma_2 = \frac{\omega\epsilon_0}{(1+\omega^2\tau^2)} \quad (5)$$

and ω is the angular frequency of the incident radiation ($\omega = 1.78 \times 10^{14}$ s⁻¹ for 10.6 μm laser beam), ϵ_0 is the permittivity of free space ($\epsilon_0 = 8.85 \times 10^{-12}$ s/Cm), τ is the relaxation time of the electrons due to collisions, and σ_0 is the dc electrical conductivity. The latter two parameters are related by

$$\sigma_0 = \frac{Ne\tau}{Bm_0} \quad (6)$$

where e is the electron charge, m_0 is the electron mass, N is the 31% electron number density and B is the ratio of effective electron mass in the lattice to actual electron mass. Following Reference (14), B/N was assumed to be independent of temperature and to have the value 5.89×10^{-24} cm³ based on 2 free electrons per atom. The temperature dependence of α , then, is completely embodied in the relaxation parameter, τ . The functional dependence $\tau(T)$ was determined from literature values for the electrical resistivity of iron for temperatures varying up to and past the melt point (15,16).

The temperature dependence of α for pure iron as calculated by the Drude theory using published resistivity data is given in Figure 6 by the solid line. The function is characterized by a reduction in slope at the Curie point (770°C) and a small jump at the melt point (1536°C). This behavior is close to the square root of that of the resistivity function. The calculated room temperature value of α turned out to be 0.03 which was 50% greater than that measured in the pulsed laser experiments. To force agreement at lower temperatures in the heat conduction analysis, the Drude theory result was scaled by a constant factor (0.66) as shown by the dashed line in Figure 6. Independent data taken with a continuous CO₂ laser on a low alloy steel indicate reasonable agreement with the scaled theory as noted by the open circles in Figure 6. An additional curve in the figure indicates a function having a jump discontinuity at the Curie point, which, although included inadvertently in some of the modeling, gave improved agreement with the data as discussed below. There is no physical basis for such a jump at low beam intensities.

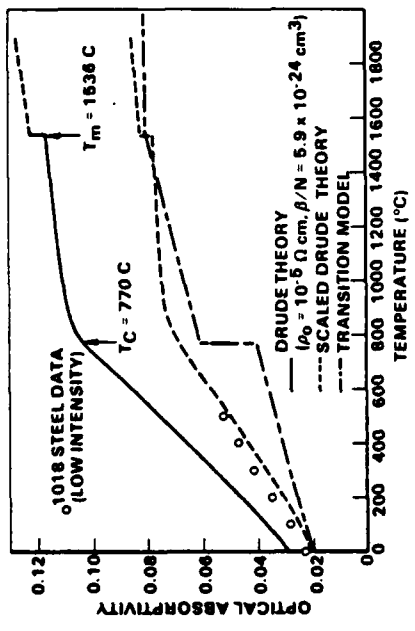


Fig. 6 - Optical absorptivity of pure iron at 10.6 μm .

Numerical calculations of the thermal response of pure iron samples to 10.6 μm laser pulses were performed using the prescribed optical absorptivity functions discussed above. Curves of effective coupling coefficient versus fluence were generated by repeating the calculation for various fluence levels and integrating the absorbed energy over the pulse length at each level. Results of the calculations are compared to the experimental data in Figures 7 and 8. The upper solid curve in Figure 7 gives the

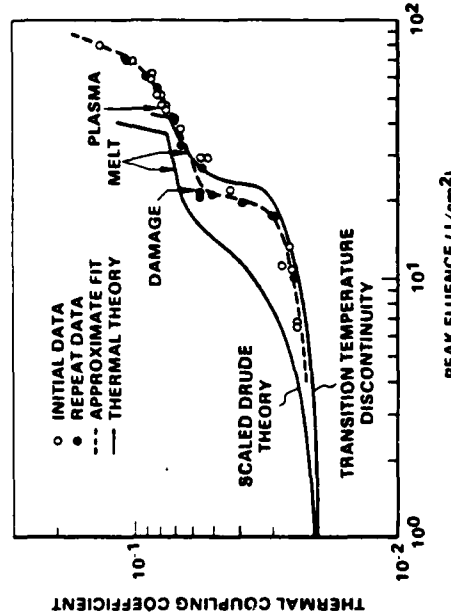


Fig. 7 - Thermal theory results for long pulse on pure iron at 10.6 μm .

computed thermal coupling for the scaled Drude theory absorption. The arrow on the curve indicates the computed melt threshold which is somewhat higher than the observed damage threshold although probably within the combined error band of the theory and experiment. The shape of the curve does not agree well with the experimental result because the theoretical coupling does not rise sharply with increasing fluence in the "shelf" region. It can

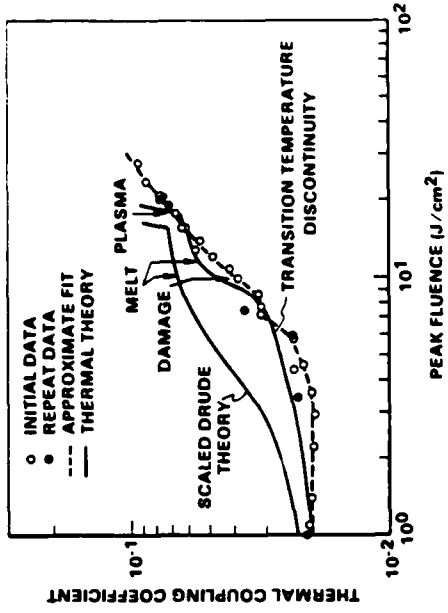


Fig. 8 - Thermal theory results for short pulse on pure iron at 10.6 μm .

be argued that some of the disagreement might arise from the fact that the theoretical result was not integrated over the spatial beam profile, however such an integration would be expected to smooth the curve rather than sharpen transition features. The lower solid curve indicates the theoretical result for the absorption model with a jump at the Curie point and surprising agreement is noted. While the jump in absorption is unphysical at low beam intensities, it might be possible for such a change to occur under intense beam conditions typical of those occurring in the experiments. Results for the short laser pulse are presented in Figure 8. Again, the theory with the jump in absorption yielded better agreement with the experiment than did the scaled Drude theory.

It is also of interest to compare the measured pure iron thermal coupling results with other experimental data to assess the extent to which the observed sharp rise in thermal coupling occurs in alloys of iron. Figure 9 presents long pulse thermal coupling data for two iron alloy samples (Fe-4.2 wt% C) taken under conditions similar to those of the pure iron irradiations. The open squares indicate data taken for a polished alloy sample. The low fluence coupling in this case is near 9% which indicates the strong effect of the alloying constituent on absorptivity. The collision frequency of the free electrons is apparently increased greatly by the presence of the carbon atoms. As fluence is increased, however, the coupling does not increase greatly, indicating that the carbon atom scattering probably dominates the pure thermal effect. As noted in the figure, the damage and plasma thresholds are lower for the alloy than for the pure material as expected. Also shown in the figure are data for a sample of the same alloy which was continuous laser homogenized from the as-cast and surface ground condition. The surface of this sample was oxidized and not free of defects as in the polished surface case. For this alloy sample (open triangles) the low fluence coupling was twice as great as that for the polished alloy. Furthermore, above the damage threshold coupling decreased with increasing fluence indicating that cleanup of the surface probably dominated any thermal effects. Also it was noted that plasma initiated below the visual damage threshold, which is typical of defect initiated plasma.

scattering when alloying constituents are added. For the alloy case, coupling is higher and much less fluence dependent.

Acknowledgments

The authors wish to thank Bernard E. Campbell and Gary L. Long for assistance in preparation of the samples and conduct of the experiments. This research was sponsored by the U.S. Army Research Office.

References

- C. T. Walters and A. H. Clauer, "Transient Reflectivity Behavior of Pure Aluminum at 10.6 μm ," *Applied Physics Letters*, 33 (8) (October, 1978) pp. 713-715.
- C. T. Walters and A. H. Clauer, "Time-Resolved Specular Reflectivity of Metals Subjected to 10.6- μm Laser Pulses," pp. 67-72 in *Laser-Solid Interactions and Laser Processing - 1978*, S. D. Ferris, H. J. Leamy, and J. M. Poate, eds.; AIP Conference Proceedings (50), Boston, Massachusetts, 1978.
- C. T. Walters, "Anomalous Behavior of the Reflectivity of Metals Irradiated with 10.6 μm Laser Pulses," pp. 98-108 in *Laser Application in Materials Processing*, J. F. Ready, ed.; SPIE 198, San Diego, California, August, 1979.
- C. T. Walters, A. H. Clauer, and B. P. Fairrand, "Pulsed Laser Surface Melting of Fe-Based Alloys," pp. 241-245 in *Rapid Solidification Processing Principles and Technologies II*, R. Mehrabian, B. H. Kear, and M. Cohen, eds.; Second International Conference on Rapid Solidification Processing, Reston, Virginia, March, 1980.
- J. F. Ready, "Change of Reflectivity of Metallic Surfaces During Irradiation by CO₂-TEA Laser Pulses," *IEEE Journal of Quantum Electronics*, QE-12 (2) (February, 1976) pp. 137-142.
- K. Ujihara, "Reflectivity of Metals at High Temperatures," *Journal of Applied Physics*, 43 (5) (May, 1972) pp. 2376-2383.
- J. A. McDordie and P. D. Roberts, "The Interaction of Pulsed CO₂ Laser Radiation with Aluminum," *Journal of Physics D: Applied Physics*, 8 (1975) pp. 768-781.
- T. J. Wieting and J. L. DeRosa, "Effects of Surface Condition on the Infrared Absorptivity of 304 Stainless Steel," *Journal of Applied Physics*, 50 (2) (February, 1979) pp. 1071-1073.
- K. Park and W. T. Walter, "Reflectance Change of a Copper Surface During Intense Laser Irradiation," pp. 274-282 in *Proceedings of the International Conference on Lasers '78*, Vincent J. Corcoran, ed., Orlando, Florida, December, 1978.

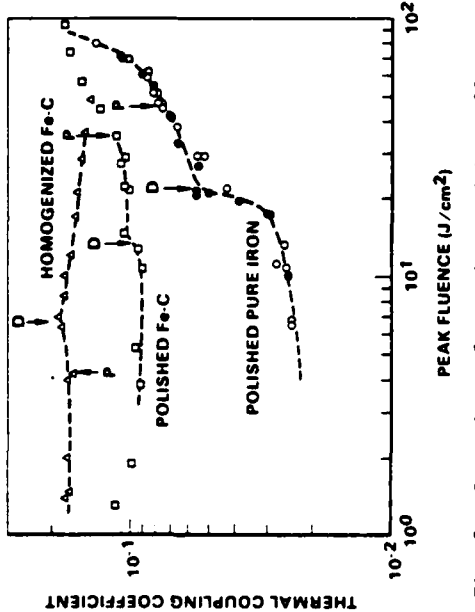


Fig. 9 - Comparison of pure iron and iron alloy thermal coupling at 10.6 μm (long pulse).

As a further check on the consistency of the alloy thermal coupling measurements, the low fluence results are compared to continuous laser measurements made on the same alloy under various conditions in Table I.

Table I. Thermal Coupling to Iron Alloy (42 C) at 10.6 μm

Condition	CW Beam (<200 C)	Pulsed Beam (Low Intensity)
Polished	0.083	0.093
Homogenized	---	0.18
Grit Blasted	0.25	---
Oxidized	0.38	---

Good agreement is noted for the polished condition. It is also clear that higher coupling is possible by surface alteration as indicated for a grit-blasted and a heavily oxidized sample. Details of the continuous laser measurements will be presented in a forthcoming paper.

Conclusions

Based on the research reported herein, it is clear that the thermal coupling coefficient for TEA CO₂ laser pulses (10.6 μm) on pure iron rises significantly with increasing fluence. This increase was more than a factor of three greater than the low fluence value for fluences less than the plasma threshold and cannot, therefore, be attributed to plasma enhancement. The details of the variation of coupling with fluence do not correlate well with a thermal model based on a simple (free electron) Drude theory but seem to require a nonlinear effect to be invoked. The sharp rise in coupling to iron with increased fluence appears to be masked by impurity

11. V. P. Ageev, A. I. Barchukov, F. V. Bunkin, V. I. Konov, S. B. Puzhaev, A. S. Silenok, and N. I. Chapliev, "Heating of Metals by CO₂ Laser Radiation Pulses," Soviet Journal of Quantum Electronics, 9 (1) (January, 1979) pp. 43-47.
12. J. A. McKay and J. T. Schriempf, "Anomalous Infrared Absorptance of Aluminum Under Pulsed 10.6 μm Laser Irradiation in Vacuum," Applied Physics Letters, 35 (6) (September, 1979) pp. 433-434.
13. Y. S. Touloukian and D. P. Devitt, Thermophysical Properties of Matter, Vol 7, Thermal Radiative Properties: Metallic Elements and Alloys, p 1644; Plenum Publishing Corporation, New York, N.Y., 1970.
14. T. J. Wieting and J. T. Schriempf, "Free-Electron Theory and Laser Interactions with Metals," Report of NRL Progress, pp. 1-13, Naval Research Laboratory, Washington, D.C., June, 1972.
15. R. W. Powell, "LXXX. The Electrical Resistivity of Liquid Iron," Philosophical Magazine, Ser. 7, 44 (354) (July, 1953) pp. 772-775.
16. H. J. Güntherodt, E. Hauser, H. U. Kunzli, and R. Müller, "The Electrical Resistivity of Liquid Fe, Co, Ni and Pd," Physics Letters, 54A (4) (September, 1975) pp. 291-292.
17. D. J. Gallant, "Temperature Dependence of the Optical Absorption in Metals," thesis presented to the Faculty of the Graduate School of the University of Southern California, June, 1980 (unpublished).

MICROSTRUCTURES OF LASER SURFACE MELTED
WHITE AND GRAY CAST IRONS

by

T. R. Tucker, A. H. Clauer, and J. L. McCall

ABSTRACT

Iron-carbon-silicon alloys containing 4.2 weight percent carbon and either 1.0 weight percent Si (gray cast) or no silicon (white cast) were laser surface melted with both continuous and pulsed CO₂ lasers. The microstructures and phases in heat affected zones and fusion zones were analyzed and compared to the as-cast starting material. The laser treatment conditions included slowly scanned homogenizing passes producing melts from 50 to 500 μm deep and pulsed irradiation melting producing layers 5-7 μm thick. The homogenizing treatment on the gray cast produced refined white cast surface structures; the same procedure applied to white cast starting materials produced more refined structures which were with the underlying material. The pulsed irradiation melts caused the formation of the ϵ supersaturated carbon phase but generally had featureless microstructures.

- Published in Microstructural Science, Vol. 10, ed. by W. E. White and J. H. Richardson, Elsevier Sci. Publ. Co., New York (1982), pp. 347-358.

microns, and it is possible to achieve extremely high rates of substrate quenching.

Laser surface treatment has been examined as a method for obtaining refinement in the microstructure at the surface, chemical homogenization of the surface layer, and removal of inclusions. In general, several hardening mechanisms are operable. One is simply a result of the refinement of the existing structure. Another is the attainment of harder phases, e.g., at the very high quench rates it is possible to obtain metastable phases -- in some instances even glassy phases.

Many factors influence the type of microstructures achieved. Some of the important ones are listed in Table 1. The heating rate determines how deep the melt will be and consequently how rapid the solidification will be. The amount of superheat and the heating rate together control how much convection will be present. Convection is generally present in all cases except at the very highest scan rates. The convection leads to irregularity in the surface pattern of the melt, to porosity within the melt, and is responsible for the mixing that occurs. Substructure is very important in certain classes of alloys, e.g., iron-carbon alloys. There is a strong tendency for epitaxial regrowth in virtually all cases that we have seen so far. In Fe-C alloys the form of the carbon is important--whether as graphite nodules, as graphite flakes, as carbides, or dissolved within the phases. And, the surface condition affects the microstructure that occurs.

In the present study the possible applicability of laser surface treatment was investigated as a way to modify the surfaces of white and gray cast irons -- the hope was to increase the properties of these materials so that they could be used for applications that currently are not possible. To evaluate the effect of the laser treating, the effects of the treatment on the microstructures of the materials were examined and evaluated.

RESULTS

Figure 2 shows the as-cast structure of the white cast iron included on the study. As can be seen, it contains random spherulites of graphites. The composition is essentially eutectic (i.e., 42% C). The melted zone was made with a focused laser beam at relatively modest translational speeds.

MICROSTRUCTURE OF LASER SURFACE MELTED
WHITE AND GRAY CAST IRONS

by

T. R. Tucker, A. H. Clauer, and J. L. McCall*

INTRODUCTION

The application of laser beams to metal surfaces provides a means to modify the surface properties without adversely affecting the bulk material. The process consists of melting surface layers to a controlled depth and at a controlled rate of speed using a laser beam as the energy source. As the schematic (Fig. 1) shows, the laser beam is incident on the surface at some point, either in the focused or an optically shaped condition. It is then swept across the surface producing a melt trail. Surface coverage is built up by overlapping these melt passes one after another. While the schematic shows the laser beam translating across the specimen, in practice the specimen is generally moved under the beam.

There are three general process mechanisms that are used for laser surface melting. The first uses a shaped or nearly uniform beam (several millimeters to a centimeter in diameter) which is translated relatively slowly. This produces a shallow melt that performs a homogenizing function. The second procedure uses a focused beam. Focus means the beam is smaller than a millimeter in diameter. This beam is translated rapidly over the surface. This produces a much higher rate of solidification and, in general, very shallow melts. This procedure can be used to obtain metastable phase structures on the surface. The third process was a pulsed laser, that is, a laser which yields very high energy intensities, but for only very short durations. In this procedure the beam is pulsed, that is, repeatedly applied. An area can be laser treated by producing overlapping pulses by a series of irradiations and translations. The depth of melting can be limited to less than ten

*Battelle-Columbus Laboratories, Columbus, Ohio 43201 USA.

The structure has been refined within the disc-shaped melt path. There is a thin chill zone within the area of the melt, about 15-20 microns thick, and there is a heat-affected zone about 10 microns thick just outside the boundaries of the melt. Although the structure within the melt zone has been refined, there still exists a very strong tendency for epitaxial regrowth. The structure on the left half of the melt tends to mimic the underlying structure in both shape and orientation. The right half of the melt shows a more open structure which correlates well with the underlying structure. There seems to be a fairly sharp demarcation between the two phases going right up through the original structure into the melt.

Figure 3 shows the results of a rapid quenching pass on a previously melted coupon of eutectic cast iron. The pass was made at about 1500 centimeters/second, almost one hundred times faster than the previous example. The power of the beam was at 5 kilowatts and it was focused as finely as possible. The original structure is similar to the as-cast structure except that it is slightly more refined and it appears to be slightly hypereutectic. The melt zone is the thin featureless area in the first 10 microns. Note that several cracks exist in the structure. The white cast iron shows a strong tendency to crack due to the stresses arising from the thermal gradients.

A slowly scanning broad beam was used in an attempt to homogenize the structure by eliminating some of the graphite spherulites. Figure 4 shows a small coupon, 1.5 centimeters on side, that has been treated in this manner. A beam about 11 millimeters in diameter was scanned across it at rates of about 6 centimeters a second. The melt area can be seen on the sample surface, top left. The top right shows a cross section, slightly magnified, which shows the as-cast structure. Some of the graphite spherulites within the as-cast structure can be seen. A dark region corresponding to the heat-affected zone is also present. At higher magnifications, the heat-affected zone can be seen in a little more detail. Also seen is a thin melt zone on the top. This is produced by controlling very carefully the rate of input. The melt zone here, which was only 50 microns thick, shows refinement over the original cast structure and also shows orientation relationships to the underlying structure.

If the rapid quench pass is applied over the previously described homogenization pass, the result shown in Fig. 5 is obtained. The bottom third of the figure is the original casting in a heat-affected condition; the broad middle portion is the scan melt zone showing the refined epitaxially-grown melt zone from the scan path; the very thin region in the top arises from the application of CO₂ laser pulses -- short pulses of about 1-1/2 microseconds in duration -- which were made in an overlapping fashion on the surface. The melt layer is approximately 5 microns thick (varying from about 3 to 7 microns over the whole surface of the piece).

Figure 6 shows these structures in more detail as revealed by a scanning electron microscope. The as-cast structure can be seen in the left hand view. The primary eutectic carbides and the pearlite phase, located in between the primary carbides, can be seen. The ferrite had been etched away deeply leaving the pearlitic carbides exposed. In the heat-affected zone, on the right, the primary carbides are largely unaffected; however, the pearlite has transformed to a mixture of high carbon martensite and retained austenite. The fact that it is high carbon martensite is known by its appearance in the micrographs, by crystallographic work with X-rays, and also by microhardness measurements. This material was extremely hard in the heat-affected zone.

Figure 7 shows the melt zone resulting from the broad beam melting. A refined version of the heat-affected zone structure is seen. The primary carbides appear to have a slightly higher volume fraction, but basically the same phases are present and the hardness values are quite comparable to the hardnesses in the heat-affect zone.

The results of the laser pulses on the surface show the 5-micron thick layer which still appears featureless even at this magnification. T.E.M. and X-ray work on this layer revealed it to consist of a cellular structure, containing primarily of a saturated phase, epsilon phase (a metastable phase containing about 4.2 weight percent carbon, about the same as in the original composition in the casting). Microhardness values of the rapidly quenched zone were intermediate between the values for the heat-affected zone and the original casting indicating that it

consisted of a supersaturated phase, but not a superhard phase like high carbon martensite.

Figure 8 shows the microstructure of a gray cast iron coupon which was exposed to laser treatment. The main difference here is that the material contains about 1 percent silicon and it was cast in a more conventional manner, causing graphite flakes to be the primary carbon constituent. The matrix consists of a fine pearlitic structure.

Figure 9 shows the effect of applying rapid melting laser passes to this material. As seen, there is not sufficient time for the graphite flakes to melt and they are left exposed. The matrix phase, which melts and resolidifies, therefore, has a lower carbon content than it would if the carbon had been taken into solution. The graphite flakes also tend to inhibit the flow of the molten pool and therefore a very irregular melt surface is obtained.

Figure 10 shows this situation at a higher magnification and reinforces these ideas. In the upper part of the melt a dendritic phase structure can be observed. The lower half of the melt shows increasingly more acicular particles toward the heat-affected zone. This is explained by a higher content of silicon in this area caused by partitioning. There is a heat-affected zone below the light area which is predominantly the result of transformation of the matrix to martensite.

Figure 11 shows the effect of using a broad homogenizing laser pass in the gray cast iron. Shown here is a cross section of a melt zone made with a fairly broad beam, about 6 millimeters, which was translated very slowly. The melt is fairly smooth in its appearance. There is a much lower tendency to crack than was observed in the white cast iron. An undercut can be seen on the side of the melt zone that is due to convection currents driven by surface tension gradients. These are equivalent to what has been seen in weld passes. Some rapid scanning passes were made on top of this which can barely be seen in this figure.

Figure 12 shows this structure at a slightly higher magnification. There are two heat-affected zones. In the lighter zone, just below the melt, the graphite flakes have not been dissolved and it appears austenite has been retained in the matrix. In the darker zone, it appears martensite

has been formed. In the melt zone itself, it appears a white cast structure exists with more carbon spherulites being present than were present in the cast white structure. The cast structure is refined over what was seen before, but it appears to be the same basic structure. In the lower figure, a high magnification view of the central region of the upper figure, the very bottom shows the darker heat-affected zone; the central region shows the lighter heat-affected zone where the matrix is light etching, presumably because of the retention of austenite; the upper portion shows the beginning of the melt zone proper, and a very fine eutectic carbide structure can be seen. Also, a few flakes are left in that melt region. It should be pointed out that there is also a fairly large tendency to form porosity in the deeper portions of the melt because of the boiling off of carbon from the melt.

Figure 13 shows the same material at even higher magnification. The left hand view shows the boundary between the melt zone and the first heat-affected zone. The lower half shows the flakes still present with a very light matrix phase. The upper half shows the melt zone structure.

The right hand figure shows affect of the application of a rapid scanning pass to this homogenized melt zone. A fairly thin and featureless melt can be seen on top and again a transition from a eutectic type growth to a cellular growth can be observed. It should be noted also that there is an absence of cracks in the rapidly quenched zone.

CONCLUSIONS

In conclusion it has been shown that a variety of microstructures are possible with laser melting in these materials. Homogenizing melt passes applied to white cast iron results in very hard martensitic microstructures. Rapidly quenched melts of the same material produce a carbon saturated metastable phase similar to splat quenched specimens of the same alloys. Rapid laser melting of gray cast iron leaves the graphite flakes largely unaffected but tend to produce martensite in the matrix portion. Finally, homogenizing melt passes on gray cast iron produce layers of a refined white cast iron structure.

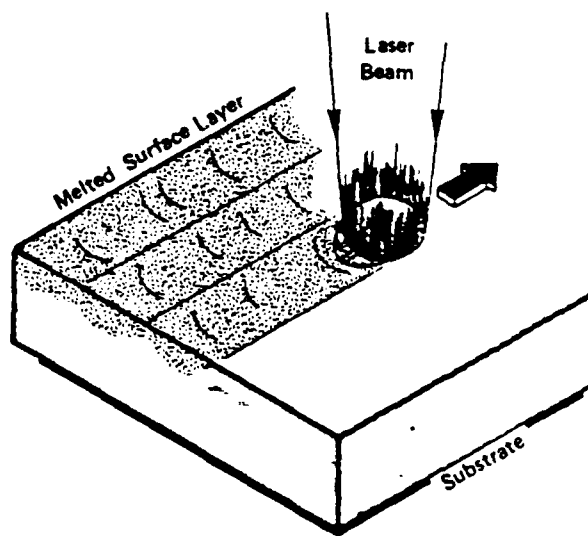


FIGURE 1. LASER SURFACE MELTING PROCESS SCHEMATIC



FIGURE 2. CONTINUOUS CO₂ LASER MELT ON WHITE CAST IRON.
A 1 KW BEAM FOCUSED TO 0.7 mm DIAMETER WITH
A 23 CM/S SCAN RATE



FIGURE 3. RAPIDLY SCANNED LASER MELT ON REFINED WHITE CAST IRON SURFACE. A FOCUSED 5 kW BEAM WITH A 1500 CM/S SCAN RATE

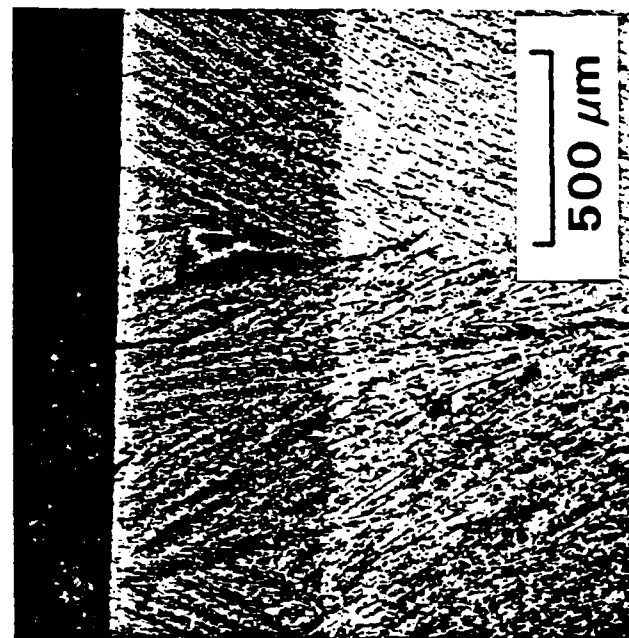
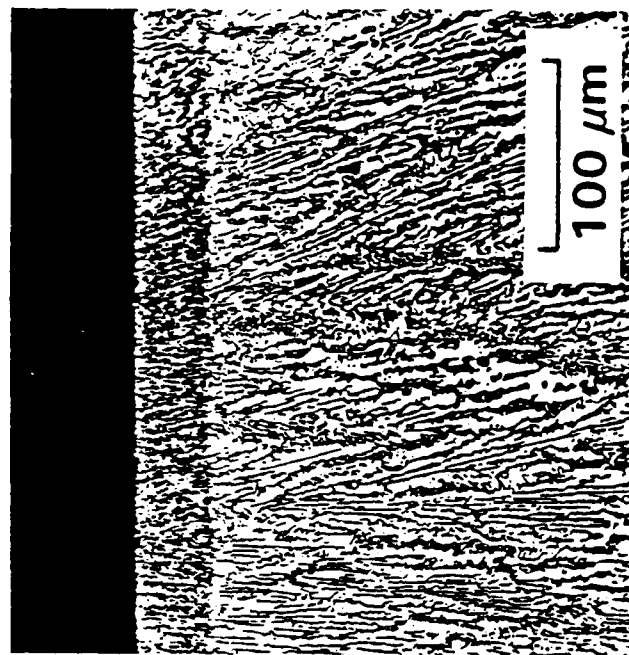
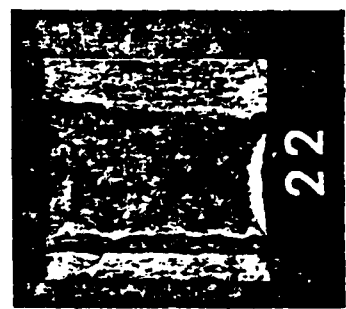
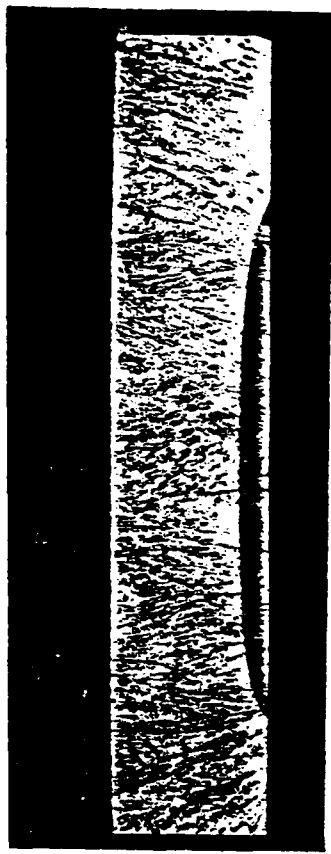


FIGURE 4. HOMOGENIZING MELT PASS ON Fe-4.2 C COUPON. A CIRCULAR BEAM 11 mm INCH DIAMETER AND 10 kW POWER SCANNED AT 6 CM/S

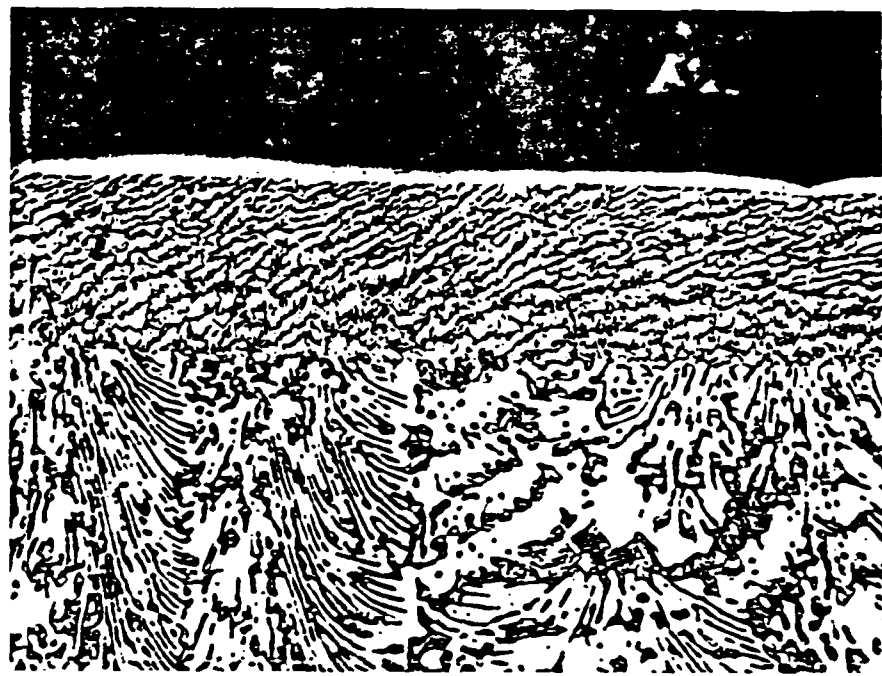


FIGURE 5. PULSED CO₂ LASER MELT APPLIED TO THE HOMOGENIZED SPECIMEN IN FIGURE 4. THE THIN FEATURELESS SURFACE LAYER AROSE FROM REPEATED PULSE IRRADIATIONS



FIGURE 6. AS-CAST AND HEAT-AFFECTED-ZONE MICROSTRUCTURES OF THE HOMOGENIZED WHITE CAST IRON SPECIMEN

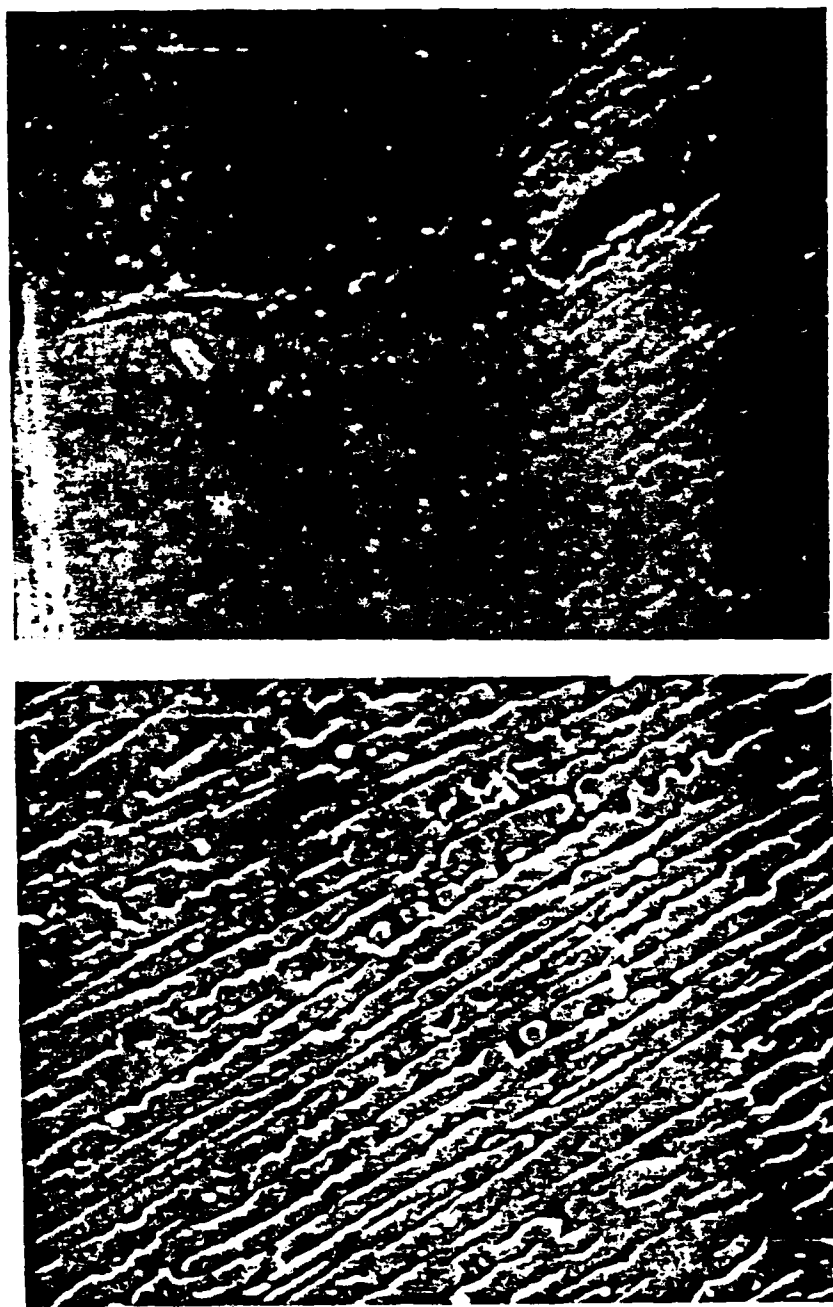


FIGURE 7. FUSION ZONE MICROSTRUCTURES FOR THE HOMOGENIZING MELT PASS (LEFT) AND PULSED LASER MELT (RIGHT)

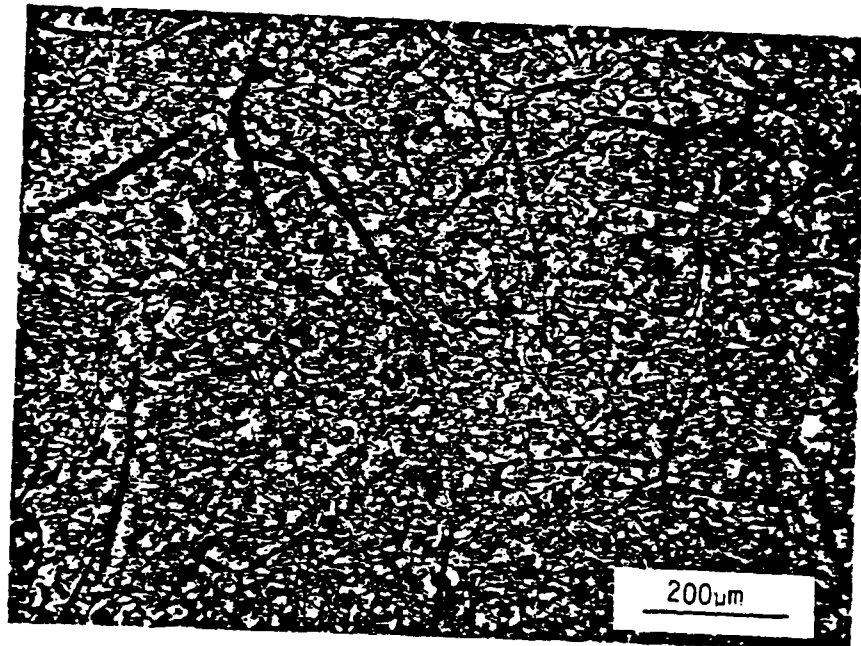


FIGURE 8. GREY CAST IRON STRUCTURE

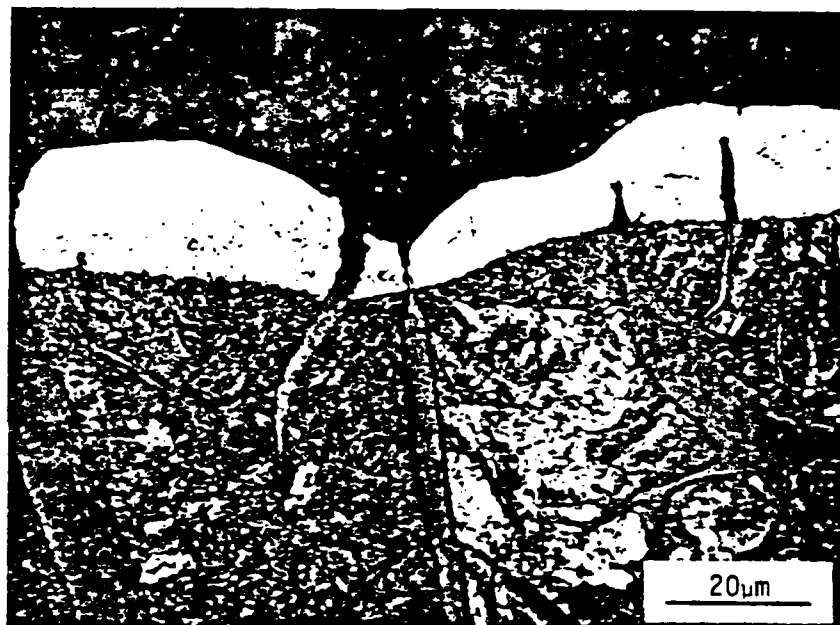


FIGURE 9. RAPID-QUENCHING LASER MELT PASSES ON GRAY CAST IRON SUBSTRATE



FIGURE 10. LASER MELTED REGION SHOWING A ZONE OF ACICULAR PARTICLES AND RESIDUAL GRAPHITE FLAKES

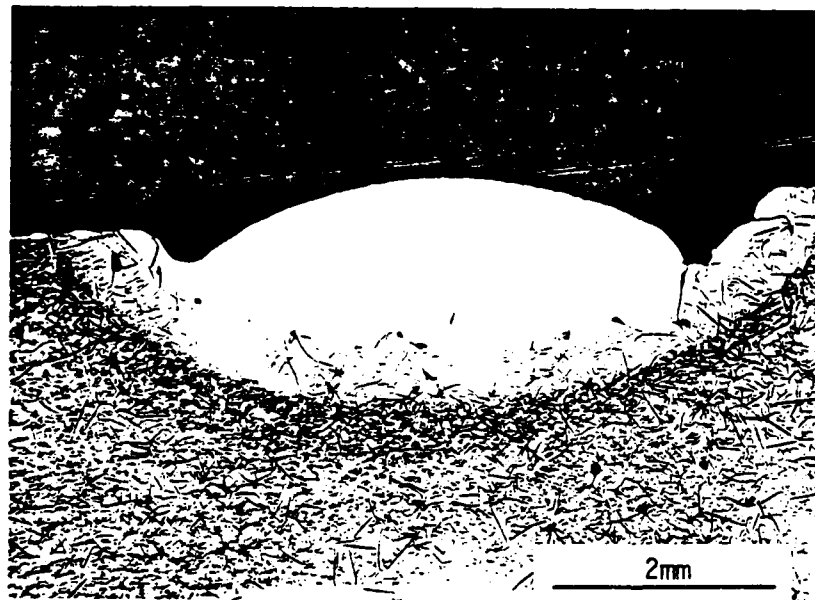


FIGURE 11. HOMOGENIZING LASER MELT PASS ON GRAY CASTING

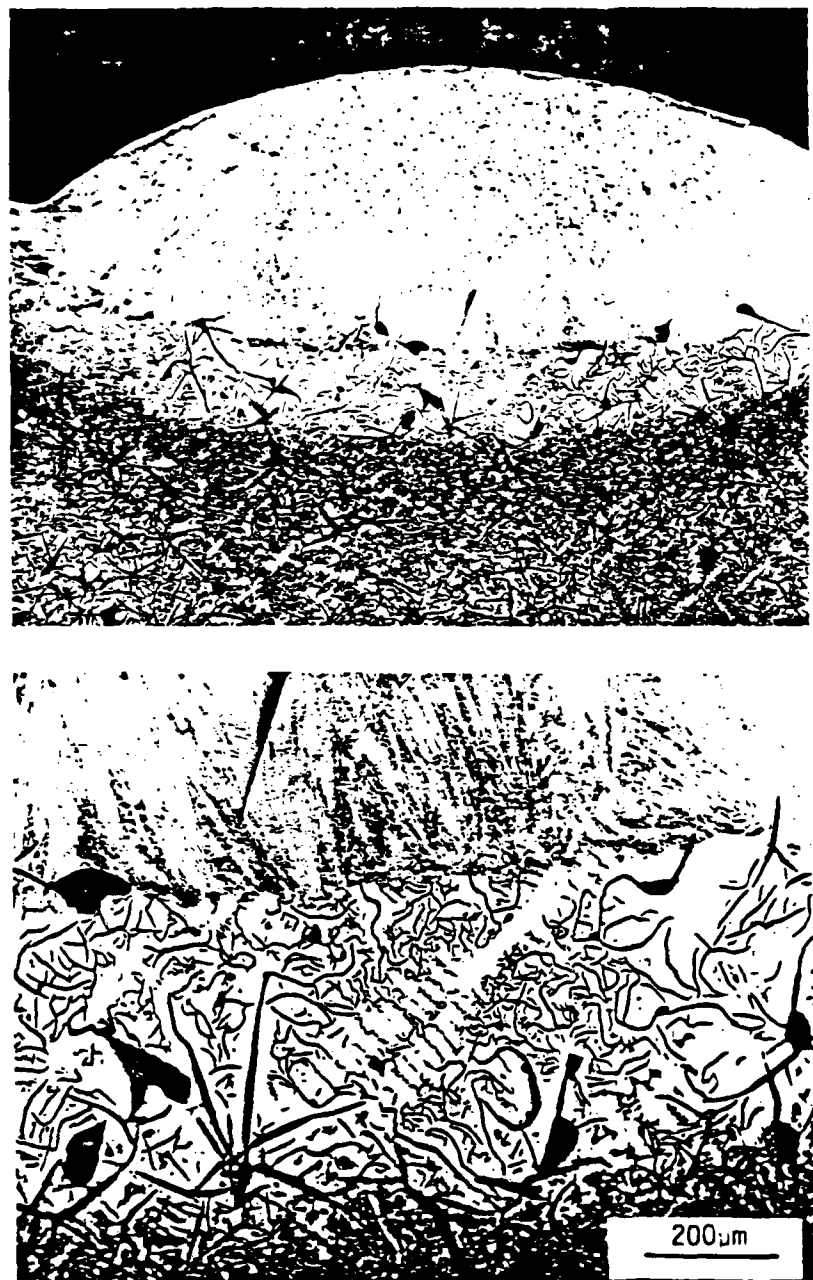


FIGURE 12. TWO HIGHER MAGNIFICATION VIEWS OF FIGURE 11
SHOWING TWO HEAT AFFECTED ZONES AND A WHITE
CAST IRON STRUCTURE IN THE FUSION ZONE

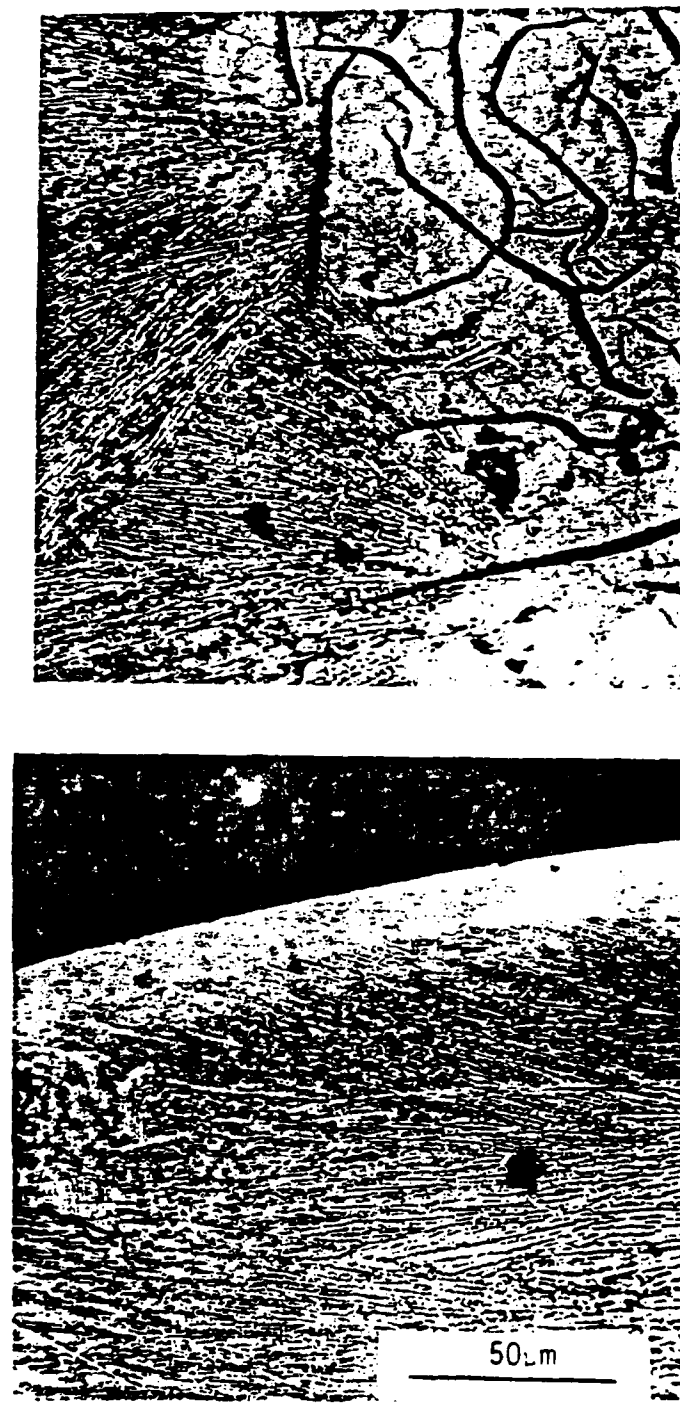


FIGURE 13. THE TRANSITION REGION BETWEEN MELT ZONE AND HAZ (UPPER)
AND A RAPIDLY QUENCHED SURFACE MELT ON THE SAME
"HOMOGENIZED" MATERIALS (LOWER)

FIGURE CAPTIONS

1. Laser surface melting process schematic.
2. Continuous CO₂ laser melt on white cast iron. A 1 kW beam focused to ~0.6 mm diameter with a 23 cm/s scan rate
3. Rapidly scanned laser melt on refined white cast iron surface. A focused 5 kW beam with a 1500 cm/s scan rate
4. Homogenizing melt pass on Fe-4.2 C coupon. A circular beam 11 mm in diameter and 10 kW power scanned at 6 cm/s.
5. Pulsed CO₂ laser melt applied to the homogenized specimen in Figure 4. The thin featureless surface layer arose from repeated pulse irradiations.
6. As-cast and heat-affected-zone microstructures of the homogenized white cast iron specimen
7. Fusion zone microstructures for the homogenizing melt pass (left) and pulsed laser melt (right)
8. Grey cast iron structure.
9. Rapid-quenching laser melt passes on gray cast iron substrate.
10. Laser melted region showing a zone of acicular particles and residual graphite flakes.
11. Homogenizing laser melt pass on gray casting
12. Two higher magnification views of Figure 11 showing two heat affected zones and a white cast iron structure in the fusion zone
13. The transition region between melt zone and HAZ (left) and a rapidly quenched surface melt on the same "homogenized" material (right)

MICROSTRUCTURES OF LASER SURFACE MELTED
WHITE AND GRAY CAST IRONS

by

T. R. Tucker, A. H. Clauer, and J. L. McCall

ABSTRACT

Iron-carbon-silicon alloys containing 4.2 weight percent carbon and either 1.0 weight percent Si (gray cast) or no silicon (white cast) were laser surface melted with both continuous and pulsed CO₂ lasers. The microstructures and phases in heat affected zones and fusion zones were analyzed and compared to the as-cast starting material. The laser treatment conditions included slowly scanned homogenizing passes producing melts from 50 to 500 μm deep and pulsed irradiation melting producing layers 5-7 μm thick. The homogenizing treatment on the gray cast produced refined white cast surface structures; the same procedure applied to white cast starting materials produced more refined structures which were with the underlying material. The pulsed irradiation melts caused the formation of the ϵ supersaturated carbon phase but generally had featureless microstructures.

RAPIDLY SOLIDIFIED MICROSTRUCTURE IN SURFACE LAYERS OF LASER- ALLOYED Mo ON Fe-C SUBSTRATES

T. R. Tucker, A. H. Clauer, S. L. Ream, and C. T. Walters
Battelle Columbus Laboratories, Columbus, Ohio 43201

ABSTRACT

Published in Rapidly Solidified Amorphous and Crystalline Alloys,
ed. by B. H. Kear, B. C. Giessen, and M. Cohen, Elsevier
Publ. Co., New York (1982), pp. 541-545.

Shaped continuous-wave laser beams have been used to alloy molybdenum coatings into Fe-C substrates. The Mo overlay was first deposited by the plasma spray process in an inert gas environment. Slowly scanned laser radiation then melted a layer 2 to 5 times the thickness of the original coating causing the two metallic species to mix. Melt proceeded from the coating/substrate interface, the Mo melt temperatures being significantly higher than that of the base material. Fusion zone microstructures for individual melt passes appeared to be homogeneous, and molybdenum composition was found to be relatively uniform. With overlapping melt passes, the microstructures became more complex with heat effects apparent in the overlap regions.

INTRODUCTION

The use of the continuous wave, high power laser as a rapid heating tool for the surface alloying of metals has been explored in a number of processes. Variations include the fusion of vapor deposited layers of Cr (1) or noble metals (2), the surface cladding of a preplaced composite powder (3), and the introduction of metallic carbides into laser surface melted layers (4). As part of a program to improve the wear properties of iron-based materials, we have studied the laser alloying of molybdenum into steels and cast irons. The objective in using Mo was to utilize its carbide stabilizing and secondary hardening properties in the same way that Mo is used in conventional tool steels.

The specific process chosen to achieve surface alloying was the deep consolidation of a pure Mo plasma-spray coating on an Fe part. That is, the laser beam was used to melt a coated metal surface to a depth greater than the original coating thickness. Plasma spray deposition was employed because it is an efficient practical method for producing the desired coating thicknesses with minimal substrate effects. A second advantage of plasma spray coating was the irregular surface finish which provided improved absorption for the far infrared laser radiation.

EXPERIMENT

Test coupons were machined from iron-carbon binary castings of 0.8, 1.4, and 2.8 w/o carbon. The 15 x 15 x 3 mm coupons were coated with molybdenum by plasma spray deposition in an argon environment. The coating thickness varied from 40 to 60 μm . The coated test pieces were laser surface melted to fuse the Mo overlay into the substrate melt layer.

The experimental configuration employed in the laser alloying procedure (Fig. 1) contained a cylindrical cup which was mounted to a linear travel stage. The top of the vessel was open to admit the converging laser beam.

Argon gas was introduced at the bottom of the test volume at flow rates of 20-50 ft³/hr. A graphite block supported the sample, absorbed any laser radiation nor incident on the test coupon, and diffused the inert gas flow.

The beam configuration shown schematically in Figure 2 was produced by reimaging the crossover point of a segmented integrating mirror. The rectangular pattern was achieved by directing the reimaged beam perpendicular to the axis of the integrating mirror. The beam distribution was nearly uniform in the short dimension and trapezoidal in the long direction. Beam size was approximately 5 x 10 mm.

The processing parameters were as follows: 3-4 kilowatts incident beam power, 6-7 mm/s samples scan rate, about 50 ft³/hr inert gas flow. The sample was translated parallel to the long axis of the laser profile with the steep intensity slope leading and the more gradual slope trailing.

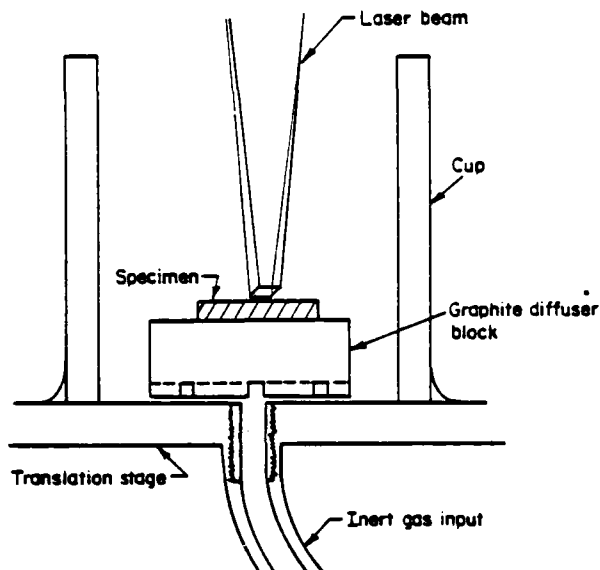


Fig. 1. Laser alloying experimental process configurations.

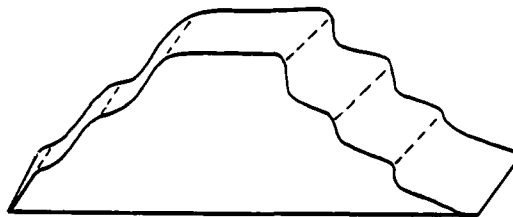


Fig. 2. Schematic representation of shaped laser optical profile.

RESULTS

Single laser melt passes employing the previously described process conditions produced uniform alloy zones as exemplified by the cross-section in Fig. 3. The alloy zones possessed refined and homogeneous microstructures which appeared to undercut the Mo coating at the melt edges. A shallower melt pass revealed more dramatically an alloy zone sandwiched between the substrate and a partially melted coating layer. Hence, the melting process must have proceeded from the coating/sample interface. This was taken to be a necessary condition for the production of uniform alloyed layers. A relatively small change in process conditions could produce a situation where melt initiated on the coating surface. In that case, less base metal melted, melt convection currents increased greatly, and alloy mixing was confined to a thin region between the two phases.

The microstructure in the alloyed zone (Fig. 4) revealed at least three phases. Initial solidification was as a two-phase structure; the surrounded phase subsequently decomposed producing acicular particles. Fig. 4A was taken from the center of the fusion zone cross-section in Fig. 3, but it was representative of the entire alloyed region. The fusion zone boundary (Fig. 4B) was intimately bonded to the substrate leaving a narrow band of material where the carbon was dissolved. There was no evidence of cracking, porosity, or delamination in the boundary region.

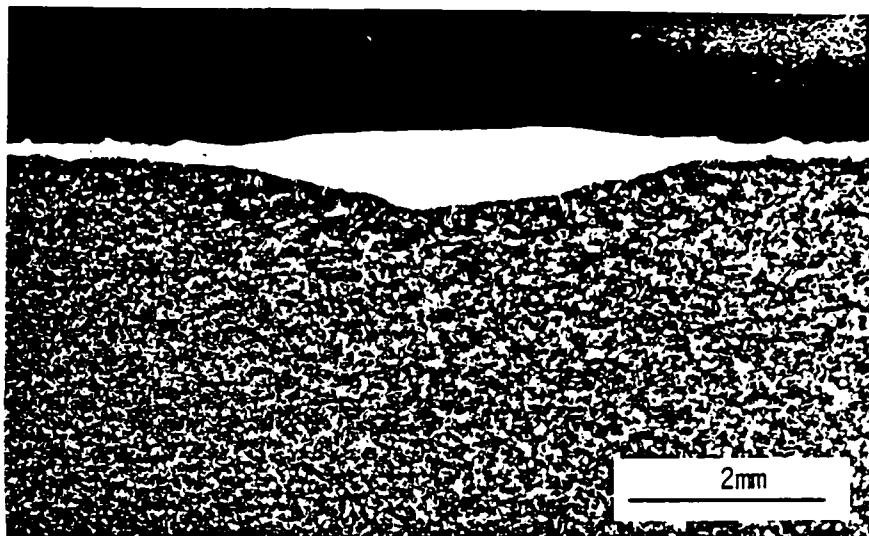


Fig. 3. Laser melt cross-section on Mo-coated Fe-0.8 C substrates.

Energy dispersive x-ray analysis was applied to this same sample to determine the relative amounts of Mo and Fe present. Three small regions within the alloyed zone were scanned for quantitative analysis. The scanned areas, which were large compared to the scale of the microstructure, were located near the middle of the width of the melt pass near the top, center, and bottom. The resulting Mo contents, ignoring any effects due to carbon, were 33.2, 27.2, and 28.7 w/o, respectively. These results were reasonable considering the depth of melt and original coating thickness.

Point analyses were also conducted on the three identifiable phases of Fig. 4A. The lighter surrounding phase measured about 34 w/o Mo, the darker regions about 15 w/o, and the particles varied between 25 and 35 w/o Mo. The particle data was an average over both the particles and the dark phase due to electron beam spreading in the sample, i.e., the effective interaction volume was larger than a single particle size. The presence of finer dispersed phases would not

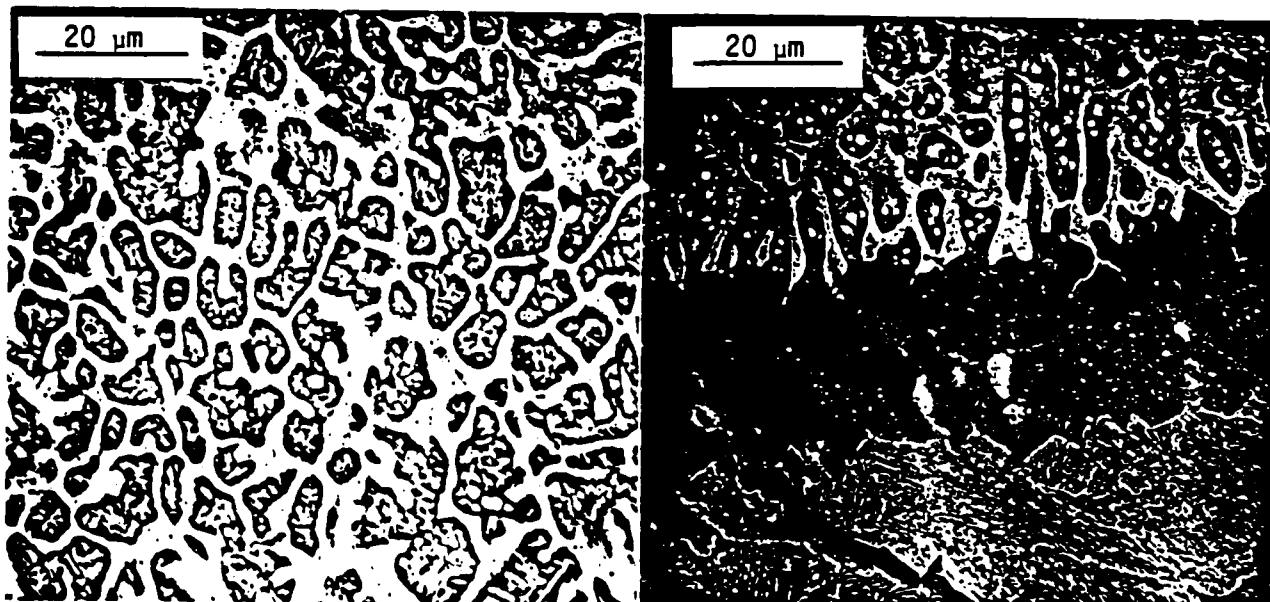


Fig. 4. Scanning electron micrograph of the cross-section in Fig. 3--A) melt zone interior, B) melt boundary.

be distinguished by this method of analysis. These limitations notwithstanding, it was surprising to find only iron-rich compositions, especially when considered on an atomic ratio basis.

The fusion zone microstructure in the Fe-1.4 C coupon (Fig. 5) revealed a dendritic solidification pattern. The darker surrounding phase was observed to be an extremely fine scale lamellar composite at high magnification. The relative Mo content of this region was equivalent to that of the surrounding phase in the previous sample. There was also a correspondence in terms of Mo weight fraction between the dendrites of Fig. 5 and the darker phase of Fig. 4A. In the case of the Fe-2.8 C substrate, a fully dendritic microstructure was obtained with colonies of dendrites possessing perpendicular side branches.

The microhardness data of Table I were averaged from a number of 500 g Knoop indents in polished sample cross-sections. The heat-affected-zone hardnesses, though greater than the corresponding as-cast data, were well below hardenability limits in each case. Solid-state cooling rates were apparently not sufficient to produce a substantial amount of martensite in the HAZ. Thus, though the solidification rate of the alloyed zone was rapid by normal casting criteria, the solid state quench rates at temperatures well below the melt point were modest.

The microhardness of the three laser-melted zones was significantly higher and remarkably similar from specimen to specimen. Measurements for the 0.8 and 1.4 C samples came from single laser melt passes, while the 2.8 C data was from multiple melt passes. Martensitic microstructures were visible in overlap regions of the third specimens. Those regions exhibited local microhardnesses exceeding 800 KHN. The overlapping pass microstructural effects resulted in wider hardness variations for the third specimen and probably a higher average value than for an equivalent single laser pass.

TABLE I
Average Knoop Hardnesses for Laser Alloyed Samples

Substrate	Casting (KHN)	HAZ	Alloyed Melt Zone
0.8 C	198	301	554
1.4 C	361	426	541
2.8 C*	416	540	604

* Overlapped laser melt passes.

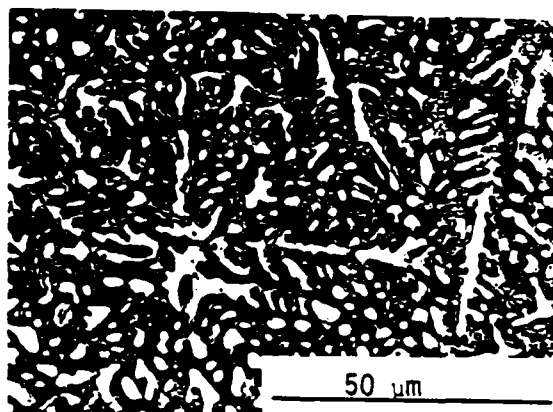


Fig. 5. Alloy zone microstructure for Fe-1.4 C substrate.

be distinguished by this method of analysis. These limitations notwithstanding, it was surprising to find only iron-rich composition, especially when considered on an atomic ratio basis.

The fusion zone microstructure in the Fe-1.4 C coupon (Fig. 5) revealed a dendritic solidification pattern. The darker surrounding phase was observed to be an extremely fine scale lamellar composite at high magnification. The relative Mo content of this region was equivalent to that of the surrounding phase in the previous sample. There was also a correspondence in terms of Mo weight fraction between the dendrites of Fig. 5 and the darker phase of Fig. 4A. In the case of the Fe-2.8 C substrate, a fully dendritic microstructure was obtained with colonies of dendrites possessing perpendicular side branches.

The microhardness data of Table I were averaged from a number of 500 g Knoop indents in polished sample cross-sections. The heat-affected-zone hardnesses, though greater than the corresponding as-cast data, were well below hardenability limits in each case. Solid-state cooling rates were apparently not sufficient to produce a substantial amount of martensite in the HAZ. Thus, though the solidification rate of the alloyed zone was rapid by normal casting criteria, the solid state quench rates at temperatures well below the melt point were modest.

The microhardness of the three laser-melted zones was significantly higher and remarkably similar from specimen to specimen. Measurements for the 0.8 and 1.4 C samples came from single laser melt passes, while the 2.8 C data was from multiple melt passes. Martensitic microstructures were visible in overlap regions of the third specimens. Those regions exhibited local microhardnesses exceeding 800 KHN. The overlapping pass microstructural effects resulted in wider hardness variations for the third specimen and probably a higher average value than for an equivalent single laser pass.

TABLE I
Average Knoop Hardnesses for Laser Alloyed Samples

Substrate	Casting (KHN)	HAZ	Alloyed Melt Zone
0.8 C	198	301	554
1.4 C	361	426	541
2.8 C*	416	540	604

* Overlapped laser melt passes.

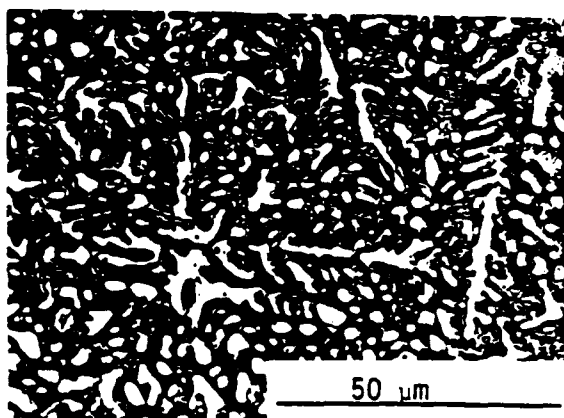


Fig. 5. Alloy zone microstructure for Fe-1.4 C substrate.

X-ray diffractometer data from the Fe-2.8 C samples alloyed surface revealed 3 prominent crystallographic phases--alloyed ferrite (BCC, $a = 2.881 \text{ \AA}$), tetragonal martensite ($c/a = 1.041$) and hexagonal carbide similar to Mo_2C . A cubic M_6C phase was also detected. The martensite, which resulted from multiple melt pass effects, contained 0.75% C as calculated from the c/a ratio. The two metallic phases were iron-related, whereas the two carbides were associated more closely with Mo.

DISCUSSION

These surface alloyed layers show significant potential for wear resistance applications. The fusion zone hardness and homogeneity are strong positive factors. Single melt pass geometry, interface bonding and macrostructure indicate no specific shortcomings in terms of overlay strength, toughness, or integrity. However, the processing of extended areas by overlapping laser passes demonstrated the need for further process development. For example, previously alloyed surface areas have a lower laser fluence threshold for melting. Therefore, the amount of overlap between laser passes influences melt depth. Additionally, the hardness and diffraction data revealed microstructural changes in the overlap zones.

While the alloy zone microhardnesses are substantial compared to normal steels, they were less than those of typical commercial tool steel products. The fact that the alloy hardesses are largely independent of substrate carbon content implies that significant hardness increases are possible. For this, two post-laser alloying processes should be considered. One approach is that surface transformation hardening treatment could be used to increase the martensite content. The other approach would be to use the laser to skin melt previously alloyed layers to retain metastable austenite. Fine scale carbides could then be precipitated from the retained austenite in a final heat treatment.

ACKNOWLEDGEMENTS

The authors wish to acknowledge the contributions of the following Battelle staff members: D. Crammer for plasma spray coating services, P. Schumacher for X-ray diffractometry, and A. Skidmore for assistance in microscopic analysis.

REFERENCES

1. L. S. Weinman, J. H. DeVault, and P. Moore, in Applications of Lasers in Materials Processing, E. A. Metzbower ed., p. 245, Am. Soc. for Metals, Metals Park, Ohio (1979).
2. C. W. Draper, C. M. Preece, D. C. Jacobsen, L. Buene, and J. M. Poate, in Laser and Electron Beam Processing of Materials, C. W. White, and P. S. Peercy eds., p. 721, Academic Press, NY (1980).
3. D. S. Gnanamuthu, in Applications of Lasers in Materials Processing, E. A. Metzbower ed., p. 177, Am. Soc. for Metals, Metals Park, Ohio (1979).
4. J. D. Ayers and T. R. Tucker, Thin Solid Films, V. 73, p. 201 (1980).

LASER SURFACE MELTING OF IRON - 4.2 WT. PCT. CARBON ALLOY*

T. R. Tucker, A. H. Clauer, C. T. Walters, S. L. Ream
Battelle Columbus Laboratories
Columbus, OH

B. P. Fairand
Laser Consultants, Inc.
Upper Arlington, OH

Continuous and pulsed CO₂ laser beams have been used to melt shallow surface layers of near-eutectic Fe-C binary alloys in the white cast condition. Broad, relatively slow scan rate laser melts eliminated free carbon inclusions and refined the as-cast microstructure. In addition to grain refinement, significant surface hardening was achieved by the retention of high-carbon martensite. The addition of 1.5 μ s laser pulses in vacuum produced thinner melts on top of the homogenized layer. The phase structures observed were equivalent to splat-quenched specimens of the same alloy composition.

Published in Lasers in Metallurgy, ed. by H. Mukherjee and J. Mazumder, The Met. Soc. of AIME, Warrendale, Pennsylvania (1981).

*This work was supported by the U.S. Army Research Office.

Introduction

While much interest has been directed at rapid solidification processing of alloys based on the iron-carbon system, relatively little fundamental research has been conducted on laser surface melting of Fe-C binary alloys. Phase structures of the binary alloys produced by splat-quenching techniques have been determined (1,2,3). Laser surface melting of carbon steels, tool steels, and cast irons has also been investigated (4,5). However, the present study seeks to survey the phase and microstructural species attainable in surface-melted layers of Fe-C binary alloys and to determine control parameters for the production of such structures.

Using the earlier rapid quenching results as a guide, the following conditions were assumed. For low-carbon alloy compositions, slight variations of well-known phases were expected in the laser-melted regions. For alloys in the cast iron range of carbon contents, unusual metastable high-carbon phases were possible. Though reference (2) reported the presence of a small amount of amorphous Fe-3.8 w/o C in vacuum splat-cooled specimens, the attainment of a metallic glass layer was considered unlikely. Since most of the novel structures and phases observed to date resulted from alloys near the eutectic composition, we have studied Fe-4.2 w/o C most extensively and have concentrated on that alloy in this paper.

In particular, two process conditions at opposite ends of the laser processing spectrum are discussed. The first process employed a high-power continuous-wave laser to melt a relatively broad region of a slowly translated coupon. The intent of the scanned melt passes was to homogenize the as-cast material and refine the grain size. In the second process, thin surface melt layers (1-10 μm) were produced under irradiation by 1.5 μs CO_2 laser pulses in vacuum.(6) The homogeneous, featureless fusion zones experienced quench rates comparable to those of the splat-quenched specimens in reference (1).

Experiment

CW Laser Melting

High-power continuous-wave CO_2 laser radiation ($\lambda = 10.6 \mu\text{m}$) was used to make continuous melt trails on specimens with a variety of surface conditions. In order to understand the energy coupling mechanisms involved and to control the melt process, experiments were conducted on thin-section coupons exposed to a very broad beam, thereby determining laser absorption coefficient as a function of specimen temperature and surface condition. While these results will be reported in the near future, the data relevant to this report are considered here.

Small square coupons 1 mm thick were prepared with various surface conditions from mirror polish to black paint. A thermocouple was installed in the center of the back surface. The coupon was supported by an alumina collar to minimize thermal conduction losses during laser heating. The front surface was protected from oxidation by a flow of helium gas which successfully controlled oxidation everywhere except at the specimen corners. An expanded CW laser beam of about 40 cm^2 area and powers of 1-5 kW flooded the specimen with a nearly uniform flux of 50-250 w/cm^2 (the specimen experienced a beam intensity that was about twice the average flux). By monitoring the specimen temperature changes during laser heating, the absorbed energy could be determined and related to the incident energy to determine the fraction absorbed.

To make the scanned laser melts, a different configuration was employed. 15 x 15 x 3 mm coupons received a SiC surface grit-blasting treatment before being mounted to a linear translation stage. The specimens were passed under a CW laser beam in a helium gas shielding environment. The Air Force Materials Lab 10 kW CO₂ laser produced a "top-hat" beam (round beam of nearly uniform cross-sectional intensity) that was focused to a diameter of 11 mm in the plane of the specimen surface. The measured power at the workpiece was 10 kW.

Surface melting occurred for sample translation speeds in the range of 2-8 cm/s. Melt depth depended strongly on the process speed with the most uniform melts achieved at 5.4 cm/s. A network of fine cracks was observed with some specimens exhibiting larger, through-thickness cracks. It should be noted that as-cast eutectic iron-carbon is extremely brittle and that no specimen preheat was employed in these tests.

Pulsed Laser Melting

For the most rapid heating-rate melts, specimens were placed on a translation stage in a chamber evacuated to approximately 5 mPa ($\sim 4 \times 10^{-5}$ mm Hg). Laser pulses from a 1.5 μ s TEA CO₂ laser were incident over areas of about 0.5 cm². The pulse consisted of a gain-switched-spike with total duration of about 100 ns and intensity about 7 times the average intensity followed by a linearly decreasing tail of nominally 1.4 μ s pulse width. Approximately 38% of the total beam energy was contained in the spike. Total laser pulse energy reaching the specimen varied up to a maximum of 50 J.

The pulse-irradiated coupons had one of three surface conditions: as-machined, polished and "homogenized" (melted by CW laser). Usually, a thermocouple monitored the specimen temperature in order to obtain absorption data. In addition, open shutter photography monitored the presence of luminous plasmas, and a photon drag detector observed the reflected 10.6 μ m radiation. Beam interaction and absorption data have been reported in more detail elsewhere in this volume⁽⁷⁾.

Individual pulse energy was increased until a clean, simply connected melt shape was observed on the specimen surface. The fluences necessary to reach this condition were invariably well above plasma initiation thresholds. Repeated pulsed melts were produced at the determined fluence level with the specimen being translated about 2 mm between shots. Thus, a point on the specimen was melted 4 or 5 times. Upon completion, the coupon contained a rapidly solidified layer that was about 5 μ m deep and extended over a 7 x 15 mm area.

Results

CW Laser Absorption

The procedure for heating the thin specimens was to irradiate with the laser for a time necessary to reach a given temperature, turn off the laser for 2 s, and then turn the laser on again for about 2 s. In this manner, the specimen cooling curve is immediately adjacent to the heating curve. A rear surface temperature profile is shown in Figure 1. Calculations indicated that the rear surface temperature was within 5°C of the front surface temperature for these heating rates. At the point where the laser was turned on for the second time, there is a negative slope corresponding to specimen cooling with the beam off and a positive slope related to the temperature rise with the beam on. The absorbed power at

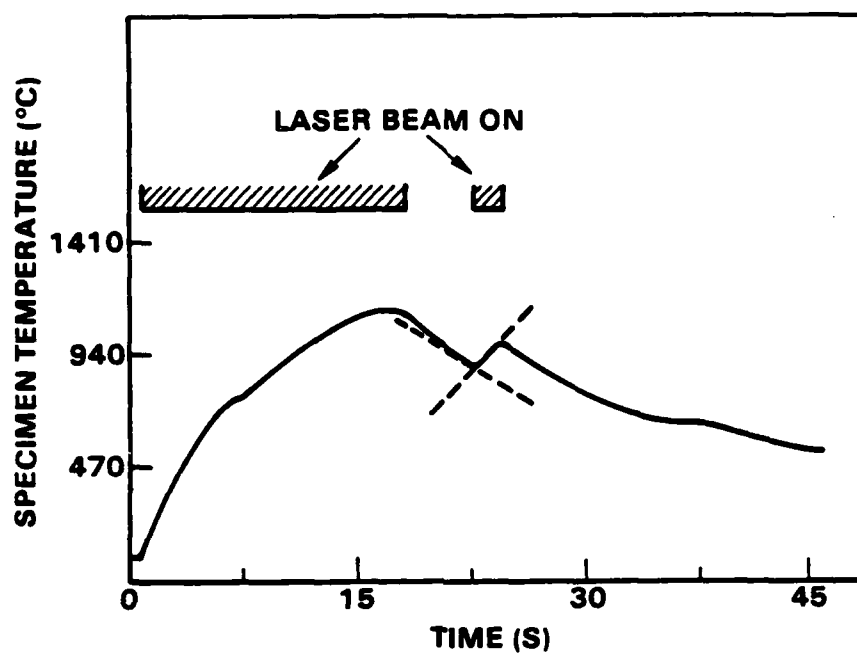


Figure 1. Temperature response of 1 mm-thick grit-blasted Fe-4.2C coupon to an expanded CW CO₂ laser beam.

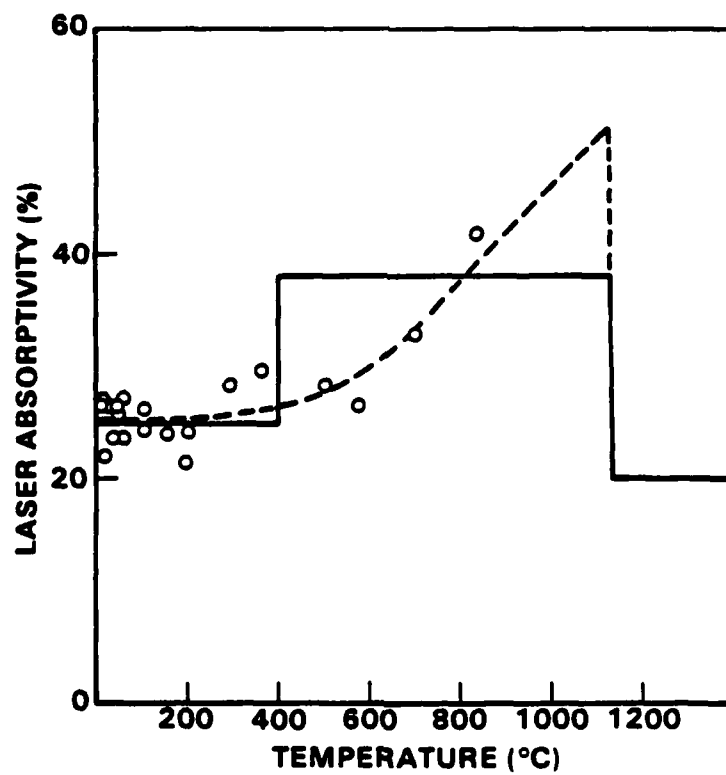


Figure 2. Thermal Coupling coefficient of specimen in Figure 1 to 10.6 μm laser radiation as a function of specimen temperature.

the specimen temperature given by the intersection of the two slopes is related to the sum of the two slopes by the following formula:

$$Q = \sigma l c \frac{dT}{dt}$$

where Q is absorbed power density in W/cm^2 , σ is density in g/cm^3 , l is specimen thickness in cm, c the specific heat in $\text{J/g}^\circ\text{C}$, and dT/dt is the specimen heating rate in $^\circ\text{C/s}$. Dividing Q by the incident power density yields the absorption coefficient.

In Figure 1, thermal arrests due to the austenitic transformation at 723°C were observed. By the formula above, the absorption coefficient depends on c which is also a function of temperature. For these experiments, c was taken to be an increasing function of temperature from 0.538 $\text{J/g}^\circ\text{C}$ at room temperature to 0.835 at the transformation point. Above that point, specific heat data show more scatter. It was assumed to hold constant at 0.835 from the transformation temperature up to the melting temperature (1130°C) in our analysis.

Figure 2 details laser absorption coefficient versus temperature for a grit-blasted surface as determined by the procedure outlined above. There is an increasing trend with temperature as shown by the dashed line. It should be noted that the room temperature average value of 25% is three times the absorptivity for a highly polished surface of the same material. The solid curve is explained in the next section.

"Homogenizing" Laser Melt Passes

Application of the scanned CW laser melting procedure to a grit-blasted coupon resulted in the structures shown in Figure 3. The $15 \times 15 \times 3$ mm specimen was translated under the 10 kW beam at 5.4 cm/s. The macro photograph of the specimen's irradiated surface reveals a glazed fusion zone that extends over more than half of the surface area. In cross-section, a dish-shaped darkened region proved to be the heat affected zone which reached a depth of 500 μm . A shallow fusion zone about 7 mm wide and 50 μm thick can be seen clearly in the lower right-hand photo of Figure 3. Substantial grain refinement has taken place in the fusion zone microstructure.

Pulsed Laser Melts

An overlapping pulsed-laser-melted cross section is presented in Figure 4. This micrograph is taken from work which was previously reported in Reference (6). The as-cast microstructure shows the familiar white cast structure consisting of the light Fe_3C phase and a darker portion corresponding to prior austenitic grains. Free carbon is present in two forms: as small particles within the darker phase network and as larger, mostly spherical inclusions.

The laser melted layer is seen as a thin featureless surface zone. The laser pulse interaction with carbon resulted in selective vaporization and particle ejection from the surface leaving a cratered morphology. A large crater appears in the center of Figure 4. These craters tended to be smoothed by the multiple pulse melts; their presence also increased the incidence of surface cracks. Crater formation during the laser pulse interaction was observed by open shutter photography as isolated luminous specks.

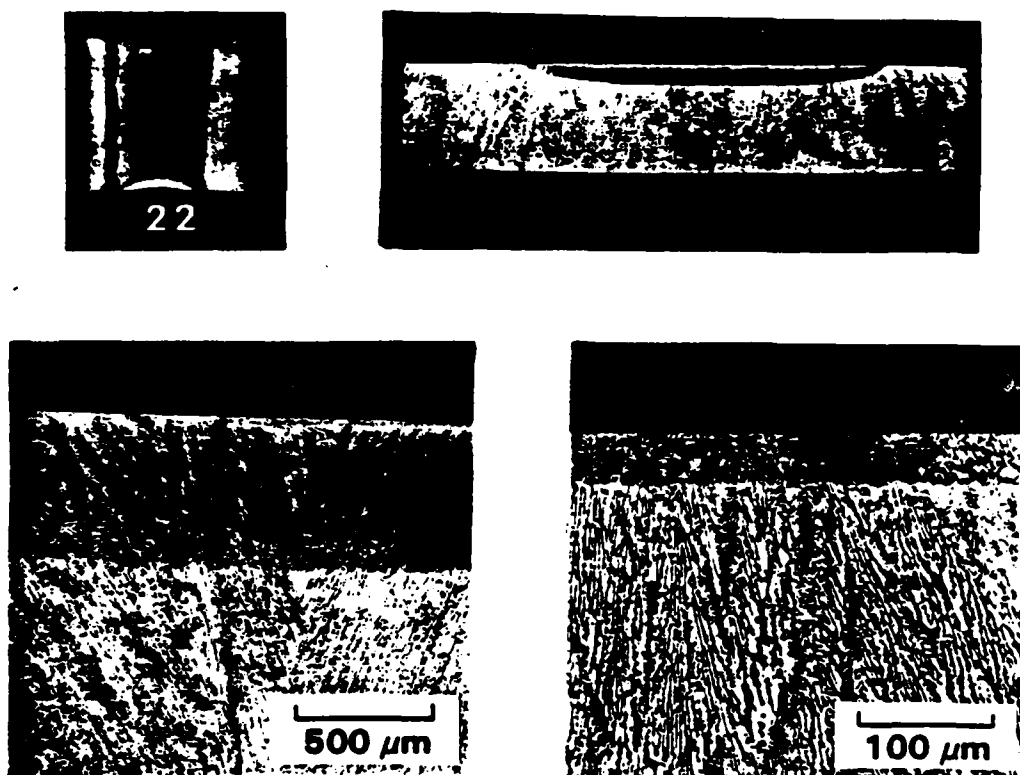


Figure 3. CW laser surface melted sample. The 15 x 15 x 3 mm grit-blasted coupon was subjected to a single 10 kW beam pass at 5.4 cm/s.

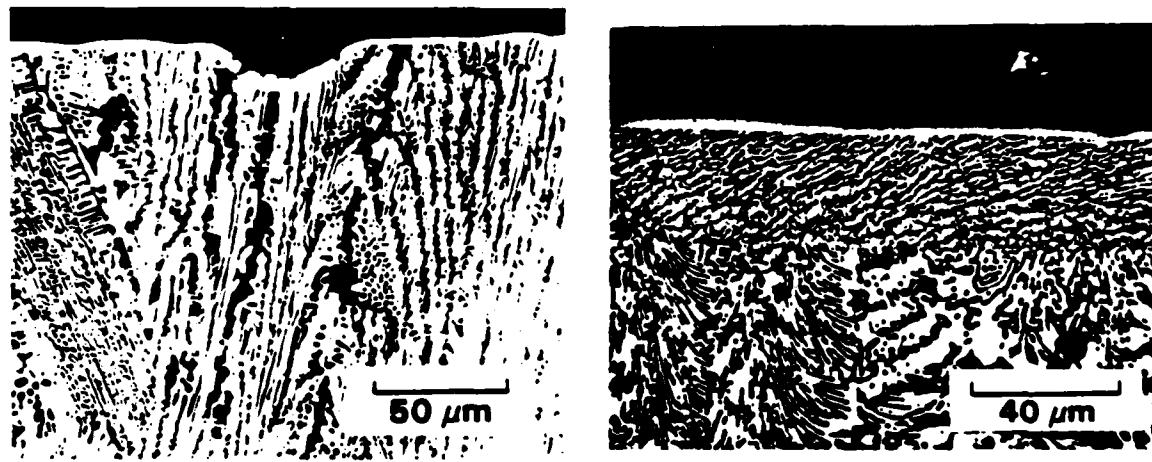


Figure 4. Overlapping TEA laser pulse surface melts on as-cast Fe-4.2C.

Figure 5. Overlapping TEA laser pulse melts on an homogenized sample. The 30 μm grain-refined area arises from the scanned CW laser pass.

Doubly Processed Surfaces

Overlapping laser pulses on homogenized coupons produced more uniform surface melts than were achieved with the original cast samples. This point is illustrated in Figure 5. There are three horizontal strata in the figure. The upper layer is the pulsed laser melted zone atop a grain-refined layer produced by the CW laser beam. The lower region is part of the heat affected zone from the scan melt pass. The homogenizing melt zone microstructure resembles the underlying structure as far as grain shape is concerned. This correspondence was observed to be true generally even for different regions of the same specimen. Thus, a strong orientation relationship between the resolidified microstructure and the substructure was inferred. This orientation appeared to take precedence over the presumed heat flow direction for a broad range of scan rates.

The pulsed laser melts on previously melted surfaces showed significantly less cratering than was observed for unhomogenized samples. This was determined by the appearance of the processed surfaces and the absence of specks in the open-shutter photographs. Surface cracking was reduced, but not eliminated entirely. The surface melt in Figure 5 has a smoother and more uniform appearance than that of Figure 4.

Properties of the various processed regions of the sample in Figures 3 and 5 are presented in Table I and Figure 6. Microhardness indents were made with a Knoop indenter under a load of either 25 g or 500 g. The indents were produced on polished cross sections with the exception of the pulsed melt data which were taken from indents of the as-melted surface. Phase analysis was accomplished by X-ray diffractometry on rectangular samples about 0.25 cm^2 in area. Filtered CuK α X-radiation which is strongly absorbed by iron was employed. The four scanning electron micrographs of Figure 6 came from approximately the same vertical section of the sample. The photos are all at the same magnification and preserve the same orientation.

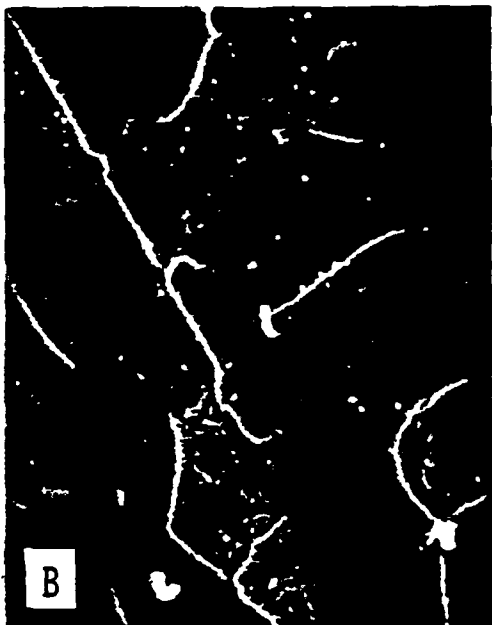
Table I. Doubly Processed Fe - 4.2C

Region	Knoop Hardness		Phases Present
	25 g	500 g	
As-cast	900	700	Fe_3C (Ortho.) α (BCC) α' (BCT) 0.35 w/o C
HAZ	1550	1100	
Scan melt	1590	--	Fe_3C (O) α' (BCT) 0.8-1.6 w/o C γ (FCC) 0.4-1.9 w/o C
Pulsed melt	1025*	--	Σ (HCP) 4.34 w/o C γ (FCC) 1.20 w/o C Fe_3C (distorted)

* Surface reading.



AS-CAST



HAZ



SCAN MELT



PULSED MELT

Figure 6. SEM micrographs of various regions in a doubly processed specimen. All photos are taken at the same magnification and orientation to the sample surface.

The as-cast structure in Figure 6A shows the lightly etched eutectic carbide phase and a deeply etched pearlitic structure. The phase determination of orthorhombic Fe_3C , ferrite, and low-carbon martensite as well as the hardness value of 700 KHN are consistent with the observed microstructure. Significant hardening was measured in the heat affected zone. This increase of more than 50% resulted in a higher hardness reading than for Fe_3C alone. The HAZ microstructure of Figure 6B shows wedge-shaped grains in the prior austenite regions. Their shape and the etching behavior suggest the presence of high-carbon martensite.

Data from the scan melt region confirmed the martensite determination. The hardness in the homogenized zone was nearly identical to that in the HAZ. Moreover, the phases detected were carbide, high-carbon martensite, and a small amount of retained austenite. The average carbon content of the martensitic phase (1.2 wt. %) correlates well to the measured microhardness value of 1100 KHN.

The microstructure of Figure 6C shows the same general appearance as the underlying structure except that the grain sizes are smaller by a factor of about five. The slanted growth direction of the scan melt microstructure extrapolates directly to the orientation of the underlying primary carbide plates in the HAZ. The scale of the homogenized layer microstructure is too small to visually determine the structure of the prior austenite grains.

For the pulsed fusion zone, a different structure was observed. The layer is featureless on the 1 μm scale of Figure 6D. Microhardness data indicate a softer structure than the underlying material, though it is probably harder than the as-cast microstructure. Phase analysis revealed the presence of the hexagonal ϵ phase, retained austenite, and dispersed carbides. The carbon content of the ϵ phase was determined by application of the formula from Reference (1) to our measured lattice parameter. The austenite exhibited a fairly narrow carbon concentration as opposed to the variations observed in the homogenizing layers. In addition, a strong orientation of the γ phase was observed with the (1,1,1) direction normal to the specimen surface. The measured value of 1.2 w/o C in the ϵ phase corresponds closely to the value of 1.18 w/o C reported by Ruhl and Cohen (1) for splat quenched Fe-4.27C.

Discussion

One surprising aspect of the scan melt regions was their shallow depth and their broad width relative to the beam diameter. Simple calculations predicted a narrower, more dish-shaped fusion zone. In this case, the explanation related to the absorption coefficient data shown in Figure 2.

A two-dimensional thermal conduction computer code with a moving heat source (ANSYS) was applied to the problem employing laser absorption coefficients represented by the solid curve in Figure 2. The code provided for temperature-dependent thermal conductivity and specific heat, but not for laser absorption. Thus, the code was run until the surface temperature reached about 400°C at which time the absorbed flux was changed manually. Another change was made when surface melting was achieved. With this set of input parameters, the calculated results confirmed observations.

Figure 7 plots the calculated and measured melt and heat affected zone profiles for the sample shown in Figure 3. The computer-calculated data were interpolated from a rather coarse calculational mesh in the

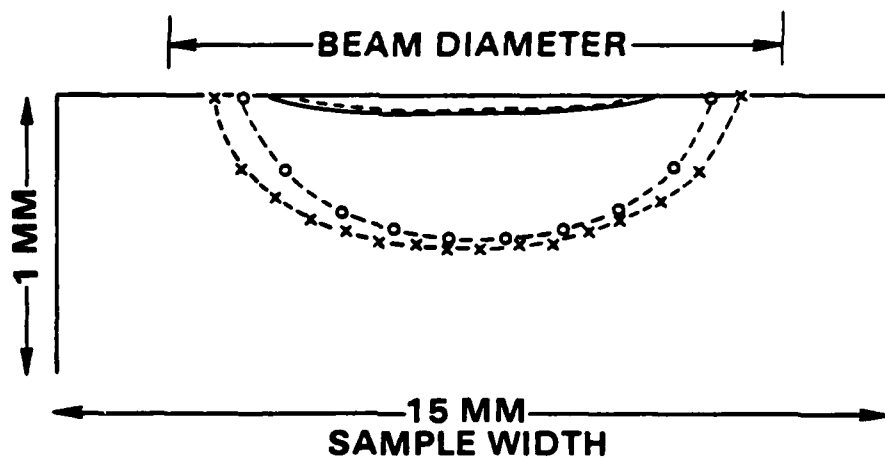


Figure 7. Melt and heat affected zone profiles for the homogenizing 10 kW laser melt pass of Figure 3.
 X = measured HAZ depth; o = calculated 730°C isotherm; solid line = measured fusion zone depth.

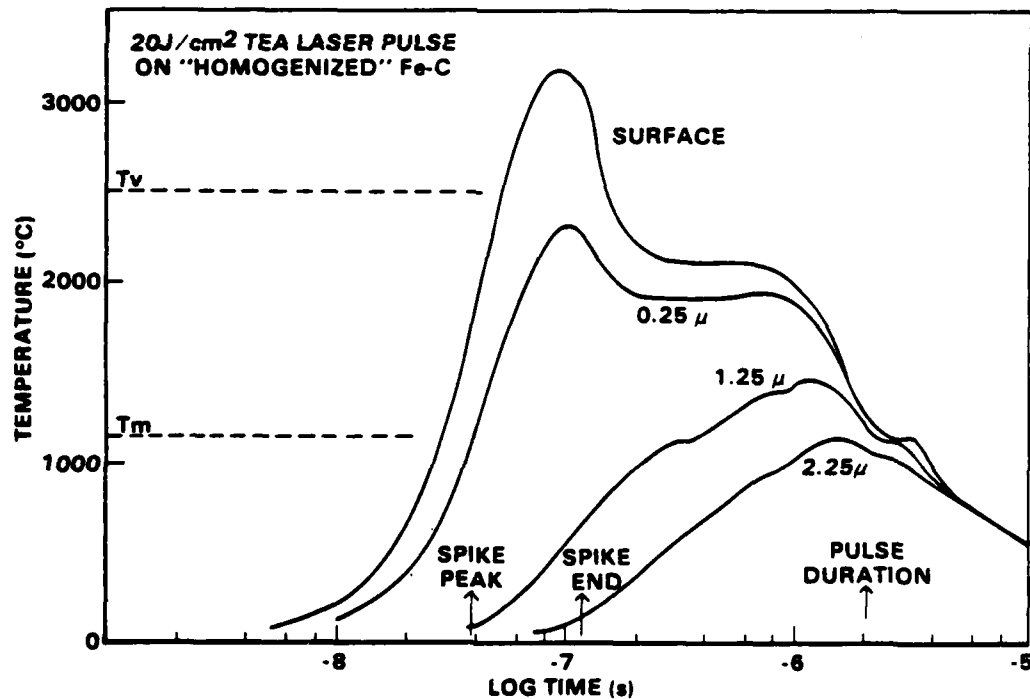


Figure 8. Calculated time-temperature profiles for different depths under the specimen surface for a 1.5 μ s pulsed laser melt on an homogenized sample.

transverse direction (1 mm) and in time (~ 20 ms). Although the calculated profiles underestimated the data by about 10%, the agreement was within expectations when the resolution of the absorption curve and calculational elements were considered. Employing the same calculations with the assumption of a constant absorbed laser flux (25% of incident average flux) resulted in peak specimen temperatures below the melt point.

Reliable experimental data for the laser coupling coefficient of the liquid alloy do not exist. However, it is reasonable to assume that the molten absorptivity would lie closer to data for polished specimens than for roughened surfaces. On this basis, a rather liberal coupling estimate of 20% was chosen for molten surfaces. The calculated results indicate that it is (1) the increase in beam absorption with temperature which allowed the surface to reach melting at the given process condition and (2) the absorption coefficient reduction on melting which tended to reduce the melt superheat. These factors combined to produce a shallow, more uniform homogenized layer than is usually achieved.

A one-dimensional finite-difference thermal absorption and conduction program was created to model the pulsed laser melting and solidification conditions. The laser pulse time history was approximated by a triangular spike followed by a linearly decreasing tail flux. Temperature-dependent laser absorption and specimen specific heat were included along with heat of fusion effects. The input beam intensity was assumed to be spatially uniform and the surface to be planar. The temperatures calculated for the uppermost calculational cells were extrapolated to the front surface for the determination of the laser absorption.

Calculated time-temperature profiles for various depths of an homogenized Fe-4.2C sample exposed to a 20 J/cm^2 laser pulse are given in Figure 8. The initial $10.6 \mu\text{m}$ absorptivity measured for the lightly oxidized surface and input to the code was 17%. The calculated melt depth for this process condition is $2.25 \mu\text{m}$. The overlapping pulsed melts of Figure 5 were produced with 50 J/cm^2 per pulse. This beam condition which produced $5 \mu\text{m}$ -deep melts is associated with a calculated melt depth of $4.25 \mu\text{m}$.

Several results can be inferred from the curves of Figure 8. First, the peak surface temperature occurs near the end of the gain-switched spike. Most of the fusion zone remains molten for 3-4 μs , during which the temperature gradient in the liquid changes dramatically. Thirdly, the cooling rates for the various depths converge below the melt point to a range on the order of $10^8 \text{ }^\circ\text{C/s}$. Finally, the speed of the solidification front can be estimated from these curves to be about 1.5 m/s .

Although the pulsed laser fusion zones appeared to be featureless in the optical and SEM micrographs, a weak cellular structure was revealed by thin-section transmission electron microscopy (TEM). The primary cell size ranged from $0.15\text{--}0.20 \mu\text{m}$ which corresponded to the grain size in the homogenized melt zones. A finer subcell structure was also observed. Additional TEM and selected area diffraction data will be required to fully determine the rapid solidification structure.

Conclusions

To summarize, continuous wave and pulsed CO_2 laser beams have been applied to binary eutectic iron-carbon samples to produce thin surface melt layers. On the basis of these results, the following conclusions may be drawn.

- (1) Changes in laser absorption due to differing surface conditions can be used to help control the melt process. In particular, increasing the absorption coefficient of the solid by surface roughening to a value higher than the molten absorptivity, tends to minimize the melt superheat and produce a uniform melt pool.
- (2) The fusion zone microstructure exhibits a strong epitaxial relationship to the substructure.
- (3) For CW laser melting at slow scan rates, the predominant hardening mechanism for Fe-4.2C is the production of high-carbon martensite.
- (4) Using 1.5 μ s laser pulses in vacuum, uniform fusion zones from 2-10 μ m in depth are produced. Calculations indicate quench rates on the order of 10^8 °C/s and an average solidification speed around 1.5 m/s.
- (5) The pulsed laser melt layers contain microcrystalline phases comparable to splat-quenched specimens of the same nominal alloy composition.

Acknowledgements

The authors wish to express gratitude to B. Campbell and G. Long of the Battelle laser lab facilities for assistance with the laser processing experiments, to H. Dooley and A. Skidmore for extensive metallographic preparation and analysis, and to P. Schumacher for the X-ray diffractometer traces.

References

1. R. C. Ruhl and M. Cohen, "Splat Quenching of Iron-Carbon Alloys", Trans. AIME, 245 (1969) pp. 241-251.
2. P. H. Shingu, K. Kobayashi, K. Shimomura, and R. Ozaki, "An Amorphous Phase in a Splat-Cooled Fe-3.8 wt. % C Alloy", Scripta Met., 8 (1974), pp. 1317-1319.
3. M. C. Cadeville, G. Kaul, M. F. Lapierre, C. Lerner, and Ph. Maitrepierre, "On Metastable Dilute Binary NiB_x and FeC_x Alloys Obtained by Splat Quenching", pp. 143-155 in Rapidly Quenched Metals, Proceedings from the Second International Conference, Section I, N. J. Grant and B. C. Giessen, eds.; MIT, Cambridge, Mass., 1976.
4. B. G. Lewis, D. A. Gilbert, and P. R. Strutt, "Laser and Electron Beam Melting of Iron-Base Hard Materials", pp. 747-753 in Laser and Electron Beam Processing of Materials, C. W. White and P. S. Peercy, eds.; Academic Press, NY, 1980.
5. P. R. Strutt, D. A. Gilbert, and H. Nowotny, "Heat Treatment of Laser Melted M2 Tool Steel", pp. 232-238 in Laser - Solid Interactions and Laser Processing - 1978, S. D. Ferris et al., eds.; American Inst. of Physics, NY, 1979.
6. C. T. Walters, A. H. Clauer, and B. P. Fairand, "Pulsed Laser Surface Melting of Fe-Base Alloys", pp. 241-245 in Rapid Solidification Processing - Principles and Technologies, II, R. Mehrabian, B. H. Kear, and M. Cohen, eds.; Claitor's Publishing Div., Baton Rouge, LA, 1980.
7. C. T. Walters, T. R. Tucker, S. L. Ream, and A. H. Clauer, "Thermal Coupling of CO₂ Laser Radiation to Metals", this volume.

Tucker, T. R., and Clauer, A. H., "Directed Energy Surface Processing of Metals". Published in Rapid Solidification Processing, Principles and Technologies, III, ed. by R. Mehrabian, B. Kear, and M. Cohen, Gaithersburg, Maryland (December 1982).

(The manuscript from this publication is not available. We will forward it when we receive it.)

END

FILMED

6-83

DTIC